Department of Physics and Astronomy

University of Heidelberg

Master thesis

in Physics

submitted by

Paula Barber Belda

born in Alzira (Spain)

2022

Strong-field effects on singly excited vibronic resonances in the hydrogen molecule.

This Master thesis has been carried out by Paula Barber Belda

at the

Max-Planck-Institut für Kernphysik in Heidelberg

under the supervision of

Prof. Dr. Thomas Pfeifer

Abstract

Studies of the hydrogen molecule interacting with ultrashort laser pulses allow for the understanding of many molecular quantum phenomena in the simplest possible molecule. In a transient-absorption experiment with H_2 in the spectral range 13-17eV, transitions from the molecular ground state to the electronically excited B, C and D states are driven by extreme-ultraviolet (XUV) light, and a second near-infrared (NIR) laser is then used to access other dark states. The aim of this project is to implement the simplest possible multi-level simulation based on light-matter interaction theory which can already reproduce the experimental results, and understand with it the importance of different excited-state couplings to the changing absorption features. The included energy levels of the eigenstates of H_2 are calculated numerically, as well as the dipole matrix elements for the considered transitions. Intensity-dependent changes in the XUV absorption spectrum in the presence of a moderately strong NIR field are observed, as well as changes in the revival time of the simulated wavepacket of the D states. In order to obtain Fano line-shaped resonances, different implementations of a predissociating continuum are examined. And finally, the effects introduced by a changing time delay between the two pulses are studied.

Zusammenfassung

Untersuchungen des Wasserstoffmoleküls und seiner Wechselwirkung mit ultrakurzen Laserimpulsen ermöglichen das Verständnis vieler quantenmolekularer Phänomene im kleinsten neutralen Molekül. In einem Transienten-Absorptionsexperiment mit H_2 im Spektralbereich 13-17eV werden Übergänge vom molekularen Grundzustand in die elektronisch angeregten B-, C- und D-Zustände durch extrem ultraviolettes (XUV) Licht angeregt, und ein zweiter Nahinfrarot-Laser (NIR) wird anschließend verwendet, um andere Dunkelzustände zu erreichen. Das Ziel dieses Projekts ist die Implementierung der einfachst möglichen Multiniveau-Simulation auf der Grundlage der Theorie der Licht-Materie-Wechselwirkung, die bereits die experimentellen Ergebnisse reproduzieren kann, und damit die Bedeutung der unterschiedlichen Kopplungen angeregter Zustände für die sich ändernden Absorptionseigenschaften verstehen. Die enthaltenen Energieniveaus der Eigenzustände von H_2 werden numerisch berechnet, ebenso wie die Dipolmatrixelemente für die betrachteten Übergänge. Es werden intensitätsabhängige Änderungen des XUV-Absorptionsspektrums in Gegenwart eines moderat starken NIR-Feldes beobachtet, ebenso wie Änderungen der Erholungszeit des simulierten Wellenpaket der D-Zustände. Um Fano-Linienresonanzen zu erhalten, werden verschiedene Implementierungen eines prädissoziierenden Kontinuums untersucht. Und schließlich werden die Auswirkungen einer wechselnden Zeitverzögerung zwischen den zwei Pulsen betrachtet werden.

List of Acronyms

B-O Born-Oppenheimer

CCD Charge-Coupled Device

CEP Carrier-Envelope Phase

FWHM Full Width at Half Maximum

HHG High-Harmonics Generation

NIR Near Infrared

OD Optical Density

SHG Second Harmonic Generation

TD Time Delay

TD-Scan Time-Delay Scan

TDDM Time-Dependent Dipole Moment

TDSE Time-Dependent Schrödinger Equation

XUV eXtreme UltraViolet

Contents

1 Introduction

Since the early development of quantum theory at the beginning of the twentieth century, the hydrogen molecule has attracted a great interest as an object of study for the scientific community. With only two nuclei and two electrons, it is the simplest neutral molecular system. Despite its relative simplicity, the four-body-motion problem describing this molecule is analytically not solvable, meaning, in the quantum case, that the Time-Dependent Schrödinger Equation (TDSE) does not have an analytical solution. Therefore, the introduction of simulations and approximations has been a very popular approach for studying this system. This approach is chosen for the following project as well.

The first laser device was built in 1960 by T. H. Maiman [1], who used ruby to create a solid-state laser. For science, engineering, medicine and surgery, the developments that followed the operation of that first ruby laser were remarkable. In particular, innovative techniques for studying and controlling dynamics of quantum systems were developed, leading to many Nobel Prizes. The most recent edition in 2022, was awarded to Alain Aspect, John F. Clauser and Anton Zeilinger. In their experiments, laser devices were used to create entangled pairs of photons, and the results establish the violation of Bell inequalities, which can be regarded as pioneering work for quantum information science [2–5].

The performance of the laser-absorption experiment, the details of which are described in [6], as well as summarized in section 2 of this thesis, gave a very particular insight in the excited-state dynamics of the H_2 molecular system. The conducted experiment studied the interaction of H_2 with two ultrashort laser pulses, in the eXtreme UltraViolet (XUV) and in the Near Infrared (NIR) regions, respectively. The experimental setup is similar to the one used in the so-called pump probe experiments, which have been widely used in the past in order to obtain direct information about the dynamics of light-matter interactions of atoms and molecules [7–12]. In pump-probe experiments, the pump pulse initiates a sample response and then, a probe pulse monitors the response, usually with a lower optical intensity that does not significantly affect the sample. However, the present experiment aims not only to observe the dynamics of the system, but also to control them. It uses an XUV laser pulse to access the excited states of the system and then, makes use of the NIR laser in order to couple those excited states to others and access dark states of the system. The experiment is in the spectral range of 13-17 eV, which has also been looked at in other previous experimental works [13–16].

Past studies have already demonstrated laser control of quantum dynamics. The dynamics of the wavepacket are observed [16–22] and coherent control is also a broad research topic [23, 24]. The revival time of the wavepacket is a common observable [25, 26]. In the present work, a wavepacket consisting in the superposition of vibrationally excited states of

the nuclear motion within the D-potential-energy curve will be reconstructed. Moreover, the possibility of changing the revival time using the NIR light is studied, combining the experimental results with the performed simulations, as will be published in [27]. The aim of the thesis is to create the most simple model simulation that can explain the key experimental results, such as line width and shape.

The thesis is structured in six chapters. After a brief introduction, the experimental details motivating the multi-level simulations performed are described in section 2. Section 3 consists in a summary of the most relevant theoretical concepts for the thesis. In section 4, the details of the multi-level simulation are described, as well as the codes used to gather the information on the energy states and the eigenvectors of the hydrogen molecule, needed for the computation of the time evolution. The results of the multi-level simulation are shown in section 5. Finally, the conclusions are presented.

2 Experimental motivation

The current work came motivated by the results of an absorption experiment with the hydrogen molecule, which will be shortly explained in the following section. For more details on the experimental setup, the reader is referred to [6].

The experiment made use of the transient absorption spectroscopy technique, as shown in fig.1. Two pulses illuminated the target, a NIR pulse (central wavelength of 780 nm) and an XUV pulse, generated by High-Harmonics Generation (HHG).

The original, short ($\sim$5fs) NIR pulse is focused on Xenon gas, generating the higher harmonics that constitute the XUV pulse. In order to regulate the intensity of the NIR field, an iris aperture is implemented, which makes use of the smaller divergence of the XUV beam, in comparison to the NIR one.

At this point, the two pulses travel together, but it is desirable to separate them, in order to study the time delay, τ, between the pulses as an experimental parameter. This is done with the interferometric spit mirror and the refocusing toroidal mirror, as indicated in fig.1, by means of using again the difference in divergence of the two beams.

The residual NIR light that was not delayed is removed using an Indium filter 200 nm thick. The combination of the mirrors and the filter completely separate the pulses, that now have a concrete and measurable time delay between them. The obtained XUV radiation spans energetically between 13 and 17 eV, in which vibronic transitions between the ground molecular state and excited electronic and vibronic states exist. The relevant transitions will be detailed in a posterior section.

These two pulses go through a second iris, in order to eliminate stray light, and hit then the H_2 target. The NIR light is filtered out and the XUV signal is detected by a Charge-Coupled Device (CCD) camera, after being dispersed by a non-linear grating. A calibration for the relationship between the energy and the position of the camera is therefore needed.

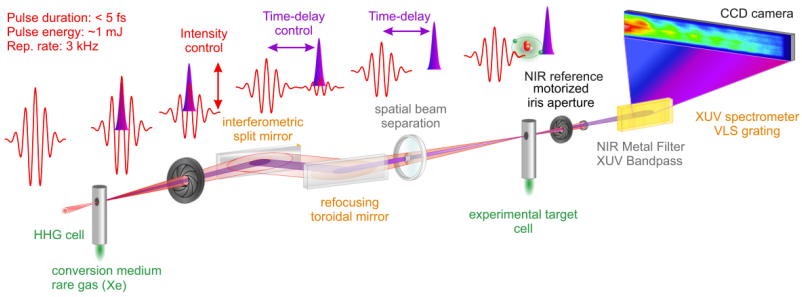

Figure 1: Experimental set-up of the absorption experiment with hydrogen target. From the original NIR pulse, another ultrashort XUV pulse is generated by HHG. The two pulses are separated in time by an interferometric split mirror and an indium filter, which removes the residual overlapping NIR radiation. The two pulses (XUV and NIR) hit the H_2 target with a time delay, τ, between them. Finally, the NIR light is filtered out, and the XUV light is projected and detected on a CCD camera. Figure from [6].

Some brief comments about the NIR pulse preparation are also presented in the following, but again the reader is to previous jobs [28] for more details. A schematic representation of the process is presented in fig.2. A 20 fs NIR pulse is s the output of a TiSa laser system consisting of an oscillator and a multi-pass amplifier, Femtopower HR/HE CEP by Femtolasers GmbH. By means of a doubly-differentially pumped hollow-core fibre, the bandwidth of the pulse is broadened, such that a broad spectrum centred at 1.6 eV is obtained. The pulse then is again compressed by being repeatedly reflected in a system of chirped mirrors. The prepared pulse has then a Full Width at Half Maximum (FWHM) of 4.7 fs and energy of about 1 mJ (the original energy of the pulse leaving the laser amplifier is 3 mJ).

Note the reader that the pulse is prepared to be Carrier-Envelope Phase (CEP) stable, meaning that the carrier and envelope peaks are locked, and there will not be a displacement between them. Experimentally, this is important for the HHG process. Moreover, since in the simulation no displacement was introduced, the simulated pulses are also CEP stable. Therefore, a greater consistency between experiment and simulation was achieved.

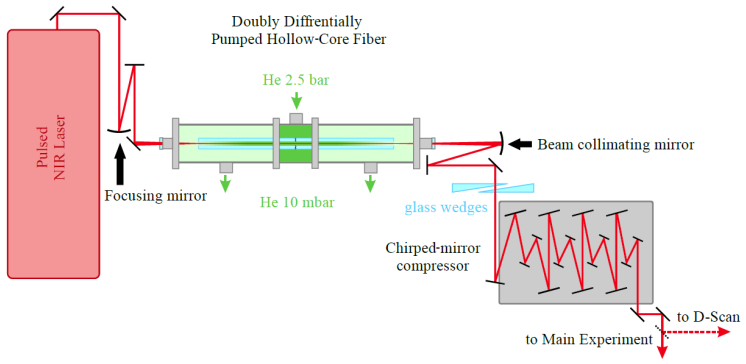

Figure 2: Scheme of the short NIR pulse preparation. The pulse is amplified in the laser cavity, band-broaded by a doubly differentially pumped hollow fibre and compressed again by a system of chirped mirrors. Figure from [28].

A typical absorption line, which could be observed in the experiment, is shown in fig.3, on the left side. On the right side, the optical density is shown for different NIR intensities. As it can be seen, incrementing the intensity of the NIR light causes line-shape changes and some lines get to be more visible. Reproducing this kind of results is the aim of the performance of the simulations, as it will be shown in the results section.

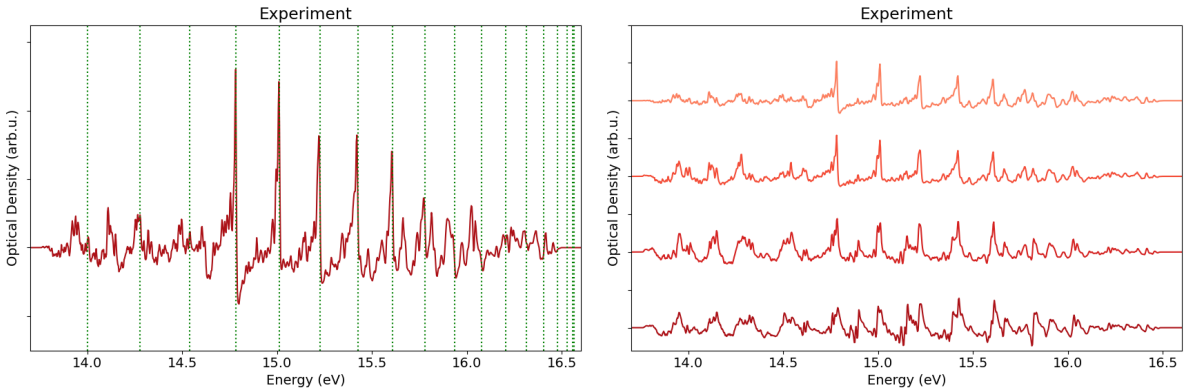

Figure 3: Example of experimentally measured spectra. On the left, one absorption spectrum measured from the experiments. In green, the theoretical values of the D energy levels can be observed. On the lower part, some more lines could be observed, which come mostly from C levels. On the right, several spectra are plot for increasing (lighter to darker) NIR intensity. The changes on the line-shape created by the NIR pulse will be investigated in the following.

Summarizing, with this experimental set-up, a transient-absorption spectroscopy experiment was realized. The results of this experiment raise interesting questions about the origin of the observed phenomena. The aim of this work will be to simulate this experimental conditions and use simplified theoretical methods in order to replicate and explain the observed results. In the next section, the relevant theoretical concepts used in the simulation will be presented.

3 Theoretical Framework

In this section, a short explanation of the relevant theoretical concepts for this work will be presented. First, the system of units used along the thesis will be described. Next, the main aspects of light-matter interaction which take place in the experiment will be exposed. Finally, a summary of the features of the particular target, the H_2 molecule is presented.

3.1 Atomic Units

Atomic units were used in this work. In this unit system, some of the relevant nature constants are set to one, such that the equations get simplified. The affected quantities are:

- The reduced Planck constant $\hbar = 1$.
- The elementary charge $e = 1$.
- The Bohr radius $a_0 = 1$.
- The electron mass $m_e = 1$.
- The quotient $\frac{1}{4\pi\epsilon_0} = 1$

In atomic units, one time unit corresponds to $t = 1\,\text{a.u.} \approx 24.189\,\text{as}$ and one energy unit, $E = 1\text{a.u.} \approx 27.211\,\text{eV}$. The intensity units follow the conversion $I = 1\,\text{a.u.} = 3.51 \times 10^{16}\,\text{W/cm}^2$ and the field strength $\mathcal{E} = 1\,\text{a.u.} = 5.142 \times 10^{11}\,\text{V/m}$.

Atomic units are usually abbreviated as "a.u.". Not to be confused with the arbitrary units, which will be referred to as "arb.u." during this work.

3.2 Light-Matter interaction

A short summary of the most important concepts when studying light-matter interaction, will be now presented. In fig.4, a schematic representation of the absorption phenomena is shown.

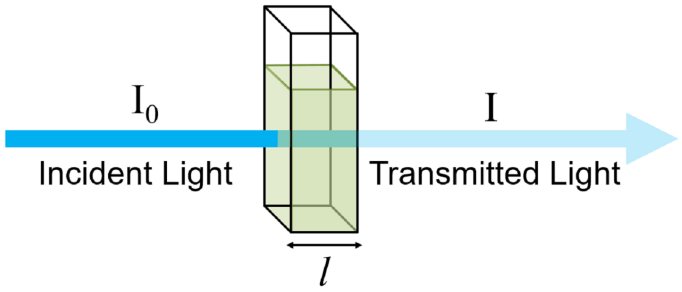

Figure 4: Schematic representation of a light beam interacting with a medium, which absorbs part of the photons that travel through it. The absorption is quantified by Lambert-Beer's law.

The experiment presented in the previous section provides as a result the intensity signal for each photon energy of the light that travelled through the medium. The most important quantity in this absorption experiments is the Optical Density (OD), which allows for the comparison of the light intensity before and after going through the medium. The Optical Density is defined as follows,

$$\mathrm{OD}(\omega) = -\log_{10}\left(\frac{I(\omega)}{I_0(\omega)}\right). \tag{1}$$

The experimental optical density was obtained using this equation. In order to do so, the reference intensity $I_0(\omega)$ needs to be defined. One way of defining the reference intensity would be to use the directly measured intensity from the experiment when no target interacts with the laser. In this case, the *absolute* optical density is measured, which has always a higher intensity than the signal with target. For the current experimental data, the reference consisted of a low pass-filtered version of the signal with the target. This produces a smooth curve, which resembles the light before the interaction. By this calculation, the so called pseudo-optical density is obtained from the measured signal and the reconstructed reference. An example of so can be seen in fig.5. This procedure does not take into account the general non-resonant absorption of light in a medium. For this reason, the signal can sometimes have a higher intensity than the reference, and the pseudo-optical density can be negative, while the absolute optical density cannot.

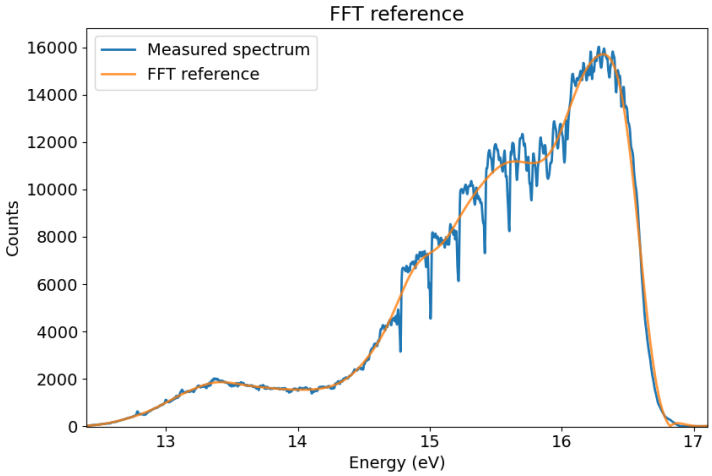

Figure 5: Measured spectrum and reference obtained by Fourier transforming the measured spectra and applying a low-pass filter. With this reference, the so-called pseudo-optical density is obtained. As it can be seen, in this case, the reference can have a smaller intensity than the measured spectrum, which leads to negative values of the pseudo-optical density.

On the one hand, the Lambert-Beer's law is considered (see fig.4), which relates the light intensity $I(\omega, z)$ after going through a medium with macroscopic absorption coefficient $\alpha(\omega)$ for a distance of interaction z and the original intensity, $I_0(\omega)$. It reads

$$I(\omega, z) = I_0(\omega) e^{-\alpha(\omega) z}. \tag{2}$$

The macroscopic absorption coefficient is related to the molecular cross-section for any particular interaction, $\sigma(\omega)$, via the number of illuminated molecules, ρ_N. The cross-section represents the probability that a molecule interacts with an incident photon of energy $\hbar\omega$. The relation is then given by

$$\alpha(\omega) = \rho_N \sigma(\omega). \tag{3}$$

Let us now on the other hand consider the wave equation of a light beam, represented by the electric field $\mathbf{E}$, propagating in homogeneous media without currents or charges

$$\left(\nabla^2 - \frac{1}{c^2}\frac{\partial^2}{\partial t^2}\right)\mathbf{E}(\mathbf{x}, t) = \mu_0 \frac{\partial^2}{\partial t^2}\mathbf{P}(\mathbf{x}, t), \tag{4}$$

where c is the speed of light in vacuum, μ_0 stands for the vacuum permeability and $\mathbf{P}(\mathbf{x}, t)$ is the linear polarization of the medium. For our particular problem, z is chosen to be the propagation direction. Therefore, the following one-dimensional equation can be used

$$\left(\frac{\partial^2}{\partial z^2} - \frac{1}{c^2}\frac{\partial^2}{\partial t^2}\right)E(z,t) = \mu_0 \frac{\partial^2}{\partial t^2}P(z,t). \tag{5}$$

The linear polarization can be obtained from the susceptibility of the medium via the following integral

$$P(z,t) = \epsilon_0 \int_0^\infty \chi(\tau)E(z,t-\tau)\,d\tau, \tag{6}$$

which, by taking a Fourier transformation on both sides, transforms in the following relation in frequency space.

$$\tilde{P}(z,\omega) = \epsilon_0 \chi(\omega)\tilde{E}(z,\omega) \tag{7}$$

In general, $\chi(\omega)$ is a tensor quantity. However, for linear, homogeneous and isotropic media, as in our case, it is a scalar quantity, and the previous relation holds.

Assuming a plane wave for the electric field and inserting this expression in equation (5), the dispersion relation can be obtained, given by

$$k^2 - \frac{\omega^2}{c^2}(1+\chi(\omega)) = 0, \tag{8}$$

where k represents the wave number. The dispersion relation is usually given as a function of the index of refraction n, which relates to the susceptibility as $n = \sqrt{1+\chi}$. Note now, that $\chi(\omega)$ is a complex quantity, which can be decomposed in its real and imaginary parts, as

$$\chi(\omega) = \chi'(\omega) + i\chi''(\omega). \tag{9}$$

In the relevant case of a diluted gas sample, $\chi(\omega)$ is some orders of magnitude smaller than unity. By Taylor-expanding and inserting the previous relation in the dispersion relation, the wave number can be approximated by

$$k \approx \frac{\omega}{c}\left(1 + \frac{\chi'(\omega)}{2} + \frac{i\chi''(\omega)}{2}\right). \tag{10}$$

The real part of the complex wave number is related to the dispersion of the medium, and the imaginary part quantifies the absorption of the medium. Therefore, the imaginary part must be related to the macroscopic absorption coefficient, and indeed, the following expression holds

$$\alpha(\omega) = \frac{\omega}{c}\chi''(\omega). \tag{11}$$

Inserting this expression in equation (3), one finally arrives to the relevant expression for the cross-section, given by

$$\sigma(\omega) = \frac{1}{\rho_N}\frac{\omega}{c}\mathrm{Im}(\chi) = \frac{\omega}{c\epsilon_0}\mathrm{Im}\big(\frac{<\mu(\omega)>}{E(\omega)}\big), \tag{12}$$

for which equation (7) was also used. $<\mu(\omega)>$ is the average dipole moment per unit volume, and its expected value is related to the Polarization $\tilde{P}(z,\omega)$, interpreted as the dipole moment per unit volume, via the number of molecules, ρ_N. The expected value of the dipole moment is the quantity that will be theoretically calculated in the simulation.

By using this result in the expression for the Lambert-Beer's law, the relevant expression for the OD is found, which reads

$$\mathrm{OD}(\omega) = -\log_{10}\left(\frac{I(\omega)}{I_0(\omega)}\right) = \frac{\sigma(\omega)}{\ln 10}\cdot\rho_N\cdot l. \tag{13}$$

As expected, the absorption of the medium is directly proportional to the cross-section of the interaction, the number of absorbers (molecules, in our case) ρ_N and the distance that the light travelled in the medium, l. From this expression, the optical density will be calculated in the simulations.

3.3 The Hydrogen molecule

This work focuses on the study of the Hydrogen molecule, H_2. Therefore, some relevant concepts about the structure and the possible transitions of the molecule in interaction with a light-field will now be presented. This section consist mostly of a summary from the works of [29].

3.3.1 Born-Oppenheimer approximation

The Born-Oppenheimer (B-O) approximation, which forms the basis of all molecular structure theory, will be briefly introduced in this section.

The key idea of the approximation is to take into account the large difference in mass between electrons (m_e) and nuclei (M),

$$\frac{m_e}{M} \sim 10^{-3}...10^{-5},$$

which causes the movement of electrons and nuclei to happen on very different timescales. In

the B-O approximation it can be considered that, on a timescale relevant for the rapid motion of the electrons, the nuclei are fixed in space.

Mathematically, this corresponds to the separation of the molecular wave function Ψ, which is a function of all the electronic ($\boldsymbol{r_i}$) and nuclei ($\boldsymbol{R}$) positions, into an electronic and a nuclear factor, meaning

$$\Psi(\boldsymbol{r_1}, \boldsymbol{r_2}, ..., \boldsymbol{r_N}, \boldsymbol{R}) = \phi(\boldsymbol{r_1}, \boldsymbol{r_2}, ..., \boldsymbol{r_N})\psi(\boldsymbol{R}) \equiv \phi(\boldsymbol{r})\psi(\boldsymbol{R}) \tag{14}$$

The sum of the kinetic energies of electrons and nuclei and the interaction potential gives the total Hamiltonian

$$H = T_n(\boldsymbol{R}) + T_{el}(\boldsymbol{r}) + V(\boldsymbol{R}, \boldsymbol{r}), \tag{15}$$

from which follows the Schrödinger equation in the form

$$\mathcal{H}\Psi(\boldsymbol{r}, \boldsymbol{R}) = [T_n(\boldsymbol{R}) + T_{el}(\boldsymbol{r}) + V(\boldsymbol{R}, \boldsymbol{r})]\Psi(\boldsymbol{r}, \boldsymbol{R}) = E\Psi(\boldsymbol{r}, \boldsymbol{R}). \tag{16}$$

The Born-Oppenheimer approximation is now applied to these equations. The electronic part of the Hamiltonian at a fixed value of $\boldsymbol{R}$ is

$$\mathcal{H}^{(el)} = H - T_n(\boldsymbol{R}) = T_{el}(\boldsymbol{r}) + V(\boldsymbol{r}; \boldsymbol{R}) \tag{17}$$

and the corresponding Schrödinger equation for the electronic part reads

$$\mathcal{H}^{el}\phi_\gamma(\boldsymbol{r}; \boldsymbol{R}) = [T_{el}(\boldsymbol{r}) + V(\boldsymbol{r}; \boldsymbol{R})]\phi_\gamma(\boldsymbol{r}; \boldsymbol{R}) = V_\gamma(\boldsymbol{R})\phi_\gamma(\boldsymbol{r}; \boldsymbol{R}), \tag{18}$$

where now $\boldsymbol{R}$ is simply a parameter. The semicolon in the electronic wave function and the potential is meant to emphasize this. Generally, there will be a set of solutions $\phi_\gamma(\boldsymbol{r}; \boldsymbol{R})$ indicated by γ, for this equation, which are the *electronic quantum numbers*. The *electronic energy* $V_\gamma(\boldsymbol{R})$ for each solution is a continuous function of $\boldsymbol{R}$ called the *molecular potential*.

In [**4**] a detailed calculation of the potentials is presented, by solving equation (18). The solution will instead be presented directly in the next section.

3.3.2 Potential curves of H_2

The most accurate way to obtain the potential curves is by experimental means. The potential energy is measured for each $\boldsymbol{R}$ position and the curve is obtained. Alternatively, one can experimentally measure the resonance energies and reconstruct the curves from the energy positions.

The equation for the Morse potential is now presented, which is the most used theoretical model to describe the potential curves. Notice the physical significance of the parameters in the expression

$$V_M(R) = E_{dis}[1 - e^{-a(R-R_0)}], \tag{19}$$

where R is the inter-nuclei separation and R_0 represents the equilibrium distance between the nuclei. E_{dis} represents the dissociation energy, meaning, the energy at which the molecule does not stay bound any more. Lastly, the parameter a allows fitting the stiffness of the potential. In fig.6 an example of a Morse potential is presented. It fits the experimental dots very well. Note also that the harmonic approximation works quite well for the first vibrational energy levels.

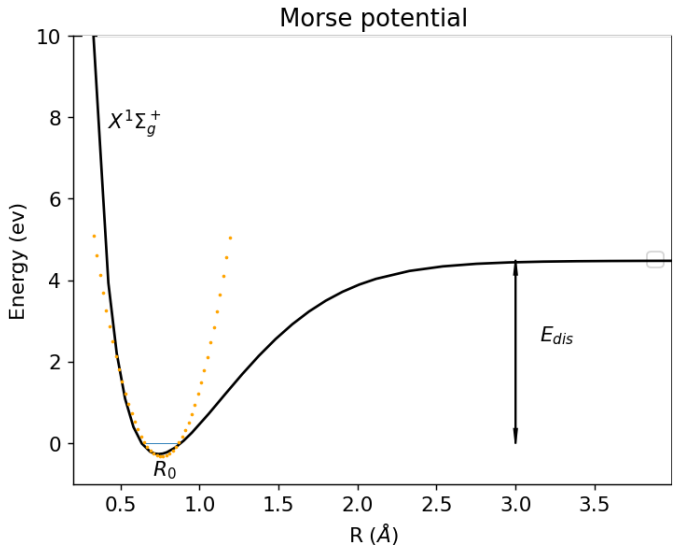

Figure 6: Example of a Morse potential to illustrate the parameters given in equation (19). In this case, it corresponds to data for the ground level of the H_2 molecule. The harmonic approximation (dashed) is also plot in the image.

The H_2 molecule is a homonuclear molecule, consisting of two atoms of hydrogen bound together. The system is composed then by two nuclei and two electrons, and it's the simplest possible neutral molecule.

In fig.7 the potentials for the most important states of the H_2 molecule are to see. The equilibrium distance of H_2 in the electronic ground state ($X^1\Sigma_g^+$) is R_0 = 0.07416 nm and the dissociation Energy E_{dis} = 4.476 eV. In the following section, the notation for the potential curves will be explained.

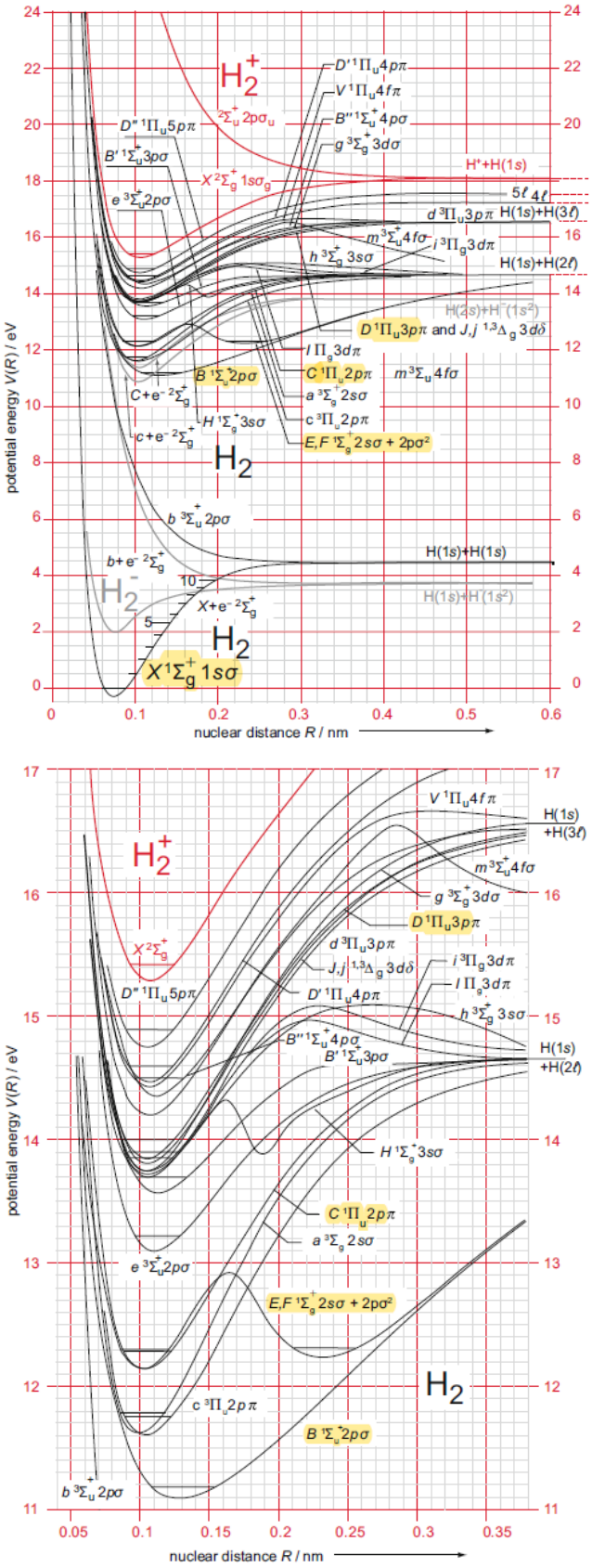

Figure 7: Potentials for the most important states of the H_2 molecule (and H_2^+ for comparison). The second plot is a zoomed version. The equilibrium distance of H_2 in the electronic ground state ($X^1\Sigma_g^+$) is R_0 = 0.07416 nm and the dissociation Energy E_{dis} = 4.476 eV. The relevant states for the current work are marked in yellow. Figure from [29].

3.3.3 Notation and symmetries

In fig.7 one can see the names of the potentials make use of a specific notation, which will be explained in the following section.

In contrast to atomic electrons, which move in a *spherically symmetric potential*, linear, homonuclear molecules must be described using *cylindrical coordinates*, taking the molecular axis as the z-axis. The assumption that the Hamiltonian does not depend on the polar angle θ and commutes with the angular momentum operator $\hat{\mathbf{L}}$ does no longer hold, and the angular momentum quantum number l is not a valid quantum number any more.

However, the projection of $\hat{\mathbf{L}}$ onto the molecular axis is still a conserved quantity, meaning that the eigenvalues of $\hat{L_z}$, m_l, are sensitive quantum numbers. Since the sign of m_l has in this case no influence on the energy, the new quantum number $\lambda = |m_l|$ is defined. λ characterizes one-electron wave functions for diatomic molecules. Parallel to the atomic designation $(s, p, d...)$ the notation shown in table 1 is used.

Table 1: Notation for the quantum number for one-electron wave functions λ.

λ	Notation
0	σ
1	π
2	δ
3	ϕ
...	...

Correspondingly, the z-component of the total orbital angular momentum is also conserved, and it is defined as

$$\hat{L_z} = \sum_i \hat{L_{zi}} \qquad \text{with eigenvalues} \quad M_L = \sum_i m_i. \tag{20}$$

One can then characterize the total molecular state with several electrons with the quantum number $\Lambda = |M_L|$ using capital Greek letters, as shown in table 2.

Table 2: Notation for the quantum number for several electrons molecular state Λ.

Λ	Notation
0	Σ
1	Π
2	Δ
3	Φ
...	...

The notation for the molecular states also refers to the total spin, S, defined as the sum of the individual spin of the electrons as

$$\hat{\mathbf{S}} = \sum_i \hat{\mathbf{S}}_i \qquad \text{with} \quad \left|\hat{\mathbf{S}}\right| = \sqrt{S(S+1)}\hbar. \tag{21}$$

Note that in this case the total spin is referred and not to the projection onto the molecular axis. For the current case of the H_2 molecule with two electrons, the sum of the two one-electron spins $S_i = \frac{1}{2}$ can result on a singlet ($S = 0$) or a triplet ($S = 1$) for the total molecular state.

One last important aspect to consider in the notation refers to the *inversion of centre of mass symmetry* of homonuclear molecules. This transformation corresponds mathematically to **r** $\rightarrow$ **-r**, or in cylindrical coordinates, $z \rightarrow -z$ and $\phi \rightarrow \phi + \pi$. Under this transformation, the states can have even "g" or odd "u" parity, as follows

$$\begin{aligned} \phi_g(\mathbf{r}) &= \phi_g(\text{-}\mathbf{r}) \\ \phi_u(\mathbf{r}) &= -\phi_u(\text{-}\mathbf{r}). \end{aligned} \tag{22}$$

Summarizing all this information, molecular states are finally denoted as

$$^{2S+1}\Lambda_{g,u}. \tag{23}$$

For example, if one looks at the ground state of the hydrogen molecule, $X^1\Sigma_g^+$, one can tell, according to equation (23), that it is a singlet state ($S = 0$) and has a total orbital angular momentum of $\Lambda = 1$. Note, here the X indicates ground state. The following states also have letters, which are alphabetically ordered with increasing energy. The + symbol here indicates that this state has a positive total *reflection symmetry*, since it results from two 1sσ, which also

have positive reflection symmetry. In the case of the Π states, positive and negative reflection symmetric states are degenerate, and this symbol is therefore left out for simplicity.

The full name of the state as can be seen in fig.7 also includes the highest in energy occupied electronic orbital of the electronic configuration (i.e. $1s\sigma$ for the ground state). Since this part is not relevant for the current work, it will be left out for the rest of the text, since the name of the states is already completely identifying the state.

Now that the molecular states have been categorized, one must also determine which transitions induced by the laser systems are allowed. The symmetry selection rules for the most probable vibrational transitions (the dipole transitions or E1 transitions) will be now stated

$$\begin{aligned} &\Delta\Lambda = 0, \pm 1 \\ &\Delta S = 0. \end{aligned} \tag{24}$$

Note that, like in the atomic case, the total electron spin is conserved in the dipole transitions, meaning that transitions between singlet and triplet states are also forbidden. In addition, the total parity of the system must be conserved. Since the photon interacting with the electron has odd parity, electronic transitions that do not change their parity are not allowed. Allowed transitions must then follow $g \to u$ or $u \to g$. This rule for centrosymmetric molecules is known as the Laporte rule. Note however that a change in the quantum number Λ does not cause a change in parity, since it constitutes the projection of the total angular momentum onto the z-axis.

Taking all that into account, and considering that our system is prepared in the ground state, the following electronic transitions are allowed

$$\begin{aligned} &X^1\Sigma_g^+ \to B^1\Sigma_u^+ \\ &X^1\Sigma_g^+ \to C^1\Pi_u \\ &X^1\Sigma_g^+ \to D^1\Pi_u \\ &\text{but} \\ &X^1\Sigma_g^+ \nrightarrow EF^1\Sigma_g^+ \end{aligned} \tag{25}$$

since no change of parity is produced in the last considered case. However, the $EF^1\Sigma_g^+$ states can be accessed from the other excited states (like $D^1\Pi_u$) by interaction with NIR photons.

Also of relevance is the vibrational nuclear quantum number ν. In the following sections, it will often be included as a subindex. This quantum number quantifies the energy level inside a potential curve, analogous to the number operator in the harmonic oscillator. In fig.7 (a), some energy levels for the ground state represented can be seen.

Note also that the rotational quantum number J is not included in this notation. Only the most likely transitions are considered, therefore only one J was considered for each of the potential curves. The most likely allowed transitions must have $\Delta J = \pm 1$. In table 3 the values for the J number for each considered state are summarized. In further research, the whole collection of rotational transitions should be considered.

Table 3: Rotational quantum numbers considered for each electronic potential curve. This decision is based on the selection rule for most likely transitions $\Delta J = \pm 1$. The ground state is considered to be in the lowest energetic state, meaning $J = 0$. The B, C and D states are accessed from the ground state, therefore, they have $J = 1$. For the EF states, it was possible to select $J = 0$ or $J = 2$, and the first option was then considered.

$X^1\Sigma_g^+$	$J = 0$
$B^1\Sigma_u^+$	$J = 1$
$C^1\Pi_u$	$J = 1$
$D^1\Pi_u$	$J = 1$
$EF^1\Sigma_g^+$	$J = 0$

3.4 Fano theory for configuration interaction

The hydrogen molecule has many potential curves, which energy states might present degeneracy. When a bound state is embedded in a continuum, the resonant line shape exhibits the so-called Fano shape, as it will be explained in this section.

This project works with a model simulation, which aims to explain the physical phenomena leading to line-shape changes in the H_2 molecule by including only the most relevant energy levels. The continuum was at first not introduced in the simulation. In this configuration, given that no NIR light is present, the absorption lines will exhibit a Lorentzian line shape, which corresponds to the Fourier transform of an exponential decay in time, as one would expect for an excitation/de-excitation process. The interaction of the H_2 molecule with the NIR photons alters this line shape. Nevertheless, since the continuum is naturally present in the system, discrepancies in the line shape between experiment and simulation are observed, which is discussed in the results section. Therefore, the introduction of the NIR pulse was not enough to explain all the details of the line shape. For this reason, configu-

ration interaction is introduced in the simulation, which transforms the Lorentzian lines into Fano lines. In this section, the most relevant theoretical concepts behind this configuration interaction are presented; and the Fano line shapes, and their relation to the Fano phases, are introduced later. This section consists of a summary of the works of Fano, [30].

Fano's theory for the configuration interaction describes the features of a quantum system, in which a bound state $|\phi\rangle$ is embedded within a set of continuum states $|\chi_E\rangle$, meaning that the energy of the bound state E_ϕ has a degeneracy with some energies of the continuum spectrum. This degeneracy causes an interaction between the bound state $|\phi\rangle$ and the continuum set of states that is not mediated by a laser field, but is instead part of the configuration of the system. This interaction causes that the states $|\phi\rangle$ and $|\chi_E\rangle$ are not eigenstates of the complete Hamiltonian of the system, but can be chosen as the basis states into which the eigenstates of the system will be expanded. The following statements hold then for the Hamiltonian of the system,

$$\langle\phi|\,\mathcal{H}\,|\phi\rangle = E_\phi, \tag{26}$$

$$\begin{aligned}\langle\chi_E|\,\mathcal{H}\,|\phi\rangle &= V_E,\\ \langle\chi_E|\,\mathcal{H}\,|\chi_{E'}\rangle &= E\,\delta(E-E'),\end{aligned} \tag{27}$$

where V_E is the configuration interaction off-diagonal matrix element which describes the non-dipole-induced interaction between the bound state and the continuum.

Let now $|\Psi_E\rangle$ be the eigenstates of the system. In the new basis, they can be expanded in terms of the old basis as

$$|\Psi_E\rangle = a_E\,|\phi\rangle + \int dE'\,b_{EE'}\,|\chi_{E'}\rangle\,, \tag{28}$$

where for the eigenstates $|\Psi_E\rangle$ is assumed that

$$\langle\Psi_E|\,\mathcal{H}\,|\Psi_E\rangle = E. \tag{29}$$

The problem consist now in the evaluation of the expansion coefficients a_E and $b_{EE'}$. The solution involves a long algebraic calculation, for which Fano's paper [30] can be used as a reference. Fano inserts the expansion of the eigenstates given in equation (28) in equation (29), which results in two equations including both coefficients a_E and $b_{EE'}$, and also uses the normalization condition

$$\langle \Psi_E | \Psi_{E'} \rangle = \delta(E - E'). \tag{30}$$

With this, he founds expressions for both coefficients, which are

$$\begin{aligned} a_E &= \frac{\sin\Delta_E}{\pi V_E}, \\ b_{EE'} &= \frac{V_{E'}}{\pi V_E} \frac{\sin\Delta_E}{E - E'} - \delta(E - E') \cos\Delta_E. \end{aligned} \tag{31}$$

where Δ_E is given by

$$\Delta_E = -\arctan \frac{\pi |V_E|^2}{E - E_\phi - F(E)} \tag{32}$$

$F(E)$ represents an energy shift, given by

$$F(E) = \mathcal{P} \int dE' \frac{|V_{E'}|^2}{E - E'}, \tag{33}$$

where $\mathcal{P}$ denotes the principal value of the integral, solving for the pole at $E = E'$.

Putting all these results together, one finds that the eigenstates can be expressed as

$$|\Psi_E\rangle = \frac{\sin\Delta_E}{\pi V_E} |\Phi\rangle - \cos\Delta_E |\chi_E\rangle , \tag{34}$$

with the *modified* bound state being

$$|\Phi\rangle = |\phi\rangle + \mathcal{P} \int dE' \frac{|V_{E'}|^2}{E - E'} |\chi_{E'}\rangle . \tag{35}$$

For convenience, a dimensionless quantity is defined to be the argument of the arctan in equation (32)

$$\epsilon = \frac{E - (E_\phi + F(E))}{\Gamma/2} = \frac{E - E_\Phi}{\Gamma/2}, \tag{36}$$

where

$$\Gamma = 2\pi |V_E|^2. \tag{37}$$

As it can be derived from equation (35), the new basis mixes the *modified* bound $|\Phi\rangle$ and the continuum $|\chi_E\rangle$ states of the original basis. Moreover, as it can be asymmetric from the

definition of the reduced energy ϵ, its expression will cause a rapid change in the expansion of the state $|\Psi_E\rangle$ around $E = E_\Phi$ within the range Γ. For this reason, $E = E_\Phi$ can be interpreted as the energy position of the *modified* bound state and Γ as its width in energy space. Note that its centre is displaced with respect to the original bound state energy resonance. As the sine and cosine functions of the reduced energy are even and odd respectively, the two states *modified* and $|\chi_E\rangle$ interfere constructively and destructively on each side of the central energy E_Φ, which causes the lines to have an asymmetric line shape.

In order to parametrize this asymmetry, the so called q-parameter is introduced, which is defined as

$$q = \frac{\langle \Phi | \hat{T} | g \rangle}{\pi V_E^* \langle \chi_E | \hat{T} | g \rangle}, \tag{38}$$

where $\hat{T}$ is the transition operator. The q-parameter corresponds to the ratio of the transition into the *modified* bound state divided by πV_E^* (corresponding to the first term in equation (34)) and the continuum states $|\chi_E\rangle$ (corresponding to the second term in equation (34)). The reason why the complex conjugate V_E^* appears is because, in order to parametrize the transition, the final bra $\langle \Psi_E |$ state is used.

The Fano line shape is then given by the following expression

$$\sigma(E) \propto \left[\frac{\left(q + \frac{2(E-E_r)}{\Gamma} \right)^2}{1 + \left(\frac{2(E-E_r)}{\Gamma} \right)^2} - 1 \right] \frac{a_E}{q^2 + 1} + b_{EE'} \tag{39}$$

and represented for different asymmetry parameters in fig.8. As it can be seen, when no configuration interaction is included ($V_E = 0$) and q tends to infinity, the lines follow a Lorentzian line shape. On the other hand, a finite value of q leads to an asymmetry in the line shape. Far from resonance ($|\epsilon| \gg 1$), the relative transition probability is approaching 1, and therefore, both sides of the resonance line tend to the same value. The Fano line shape can be measured in experiment, since it is proportional to the cross-section σ, which is the direct observable in a XUV transient-absorption experiment, related to the OD (see equation (13)).

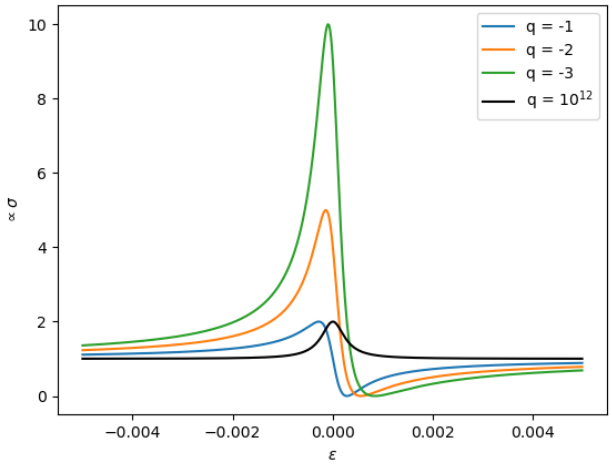

Figure 8: Examples of Fano lines for increasing q-parameter with respect to the reduced energy ϵ. A finite value of q leads to an asymmetry in the line shape. For q tending to infinity, the Lorentzian line shape is recovered.

4 Multi-level model simulation

In this section, the main features of the used simulational methods are presented. The section is divided in two parts. The first part explains the working principle of the two codes, *nucfix* and *rovib_trans* [31, 32], which were provided to us by the Saenz group. *nucfix* is used in order to get the energy levels, the eigenvectors and the nuclear wave functions for given potential curves. *rovib_trans* provides the transition probabilities between the different energy levels, in our case, vibronic levels in the hydrogen molecule.

In the second part, these "basic ingredients" are used to model the experiment explained in section 2. The fundamental quantum-mechanical concepts, the ansatz and the used approximations in the code are explained in the following.

4.1 *nucfix* and *rovib_trans*

In order to simulate the Hydrogen molecule and its interaction with two laser pulses, a deep understanding of the features of this molecule is needed, meaning the energy levels and nuclear wave functions for each electronic state, and also the transition probabilities between states.

The code *nucfix* solves numerically the nuclear part of the Schrödinger equation, in order to obtain the eigenvalues and eigenvectors, which correspond to the energy levels and nuclear wave functions, expanded on a grid of the nuclear separation variable, $\boldsymbol{R}$.

From the Born-Oppenheimer approximation section, recall that the total wave function of the system could be written as (see equation (14)),

$$\Psi(\boldsymbol{r_1}, \boldsymbol{r_2}, ..., \boldsymbol{r_N}, \boldsymbol{R}) = \phi(\boldsymbol{r_1}, \boldsymbol{r_2}, ..., \boldsymbol{r_N})\psi(\boldsymbol{R}) \equiv \phi(\boldsymbol{r})\psi(\boldsymbol{R}).$$

As it was explained in that section, the total Schrödinger equation of the system could be factorized in a nuclear and an electronic part, and each of them could be solved separately. The equation for the electronic part was then obtained. Analogously, one can focus on the nuclear part, which would read as follows

$$\mathcal{H}^{(n)}\psi(\boldsymbol{R}) = [T_n(\boldsymbol{R}) + V_\gamma(\boldsymbol{R})]\psi(\boldsymbol{R}) = E\psi(\boldsymbol{R}), \tag{40}$$

and solve for the nuclear wavefunctions $\psi(\boldsymbol{R})$ and the energy levels. In this case, $\boldsymbol{R}$ is of course not a fixed parameter. Recall, γ here stands for the (many) different electronic states.

To solve this equation, a numerical grid expansion for the potential curves $V_\gamma(R)$ was needed. This would be equivalent to solve equation (18) before calculating the nuclear part. Instead, values from literature are used, in particular, the ones provided by [33].

nucfix solves equation (40) in a box using a decomposition in B-splines, which details are beyond the scope of the project. A basis of 600 B-splines and a box of size 24 a.u. $\sim$ 12 $\mathring{A}$ were used for the calculation. From it, the set of energy levels $\{E_i\}$ and nuclear wave functions $\{\psi_i(\boldsymbol{R})\}$ needed to simulate the molecule are obtained. In fig.9 the results from *nucfix* for different relevant energy levels are presented.

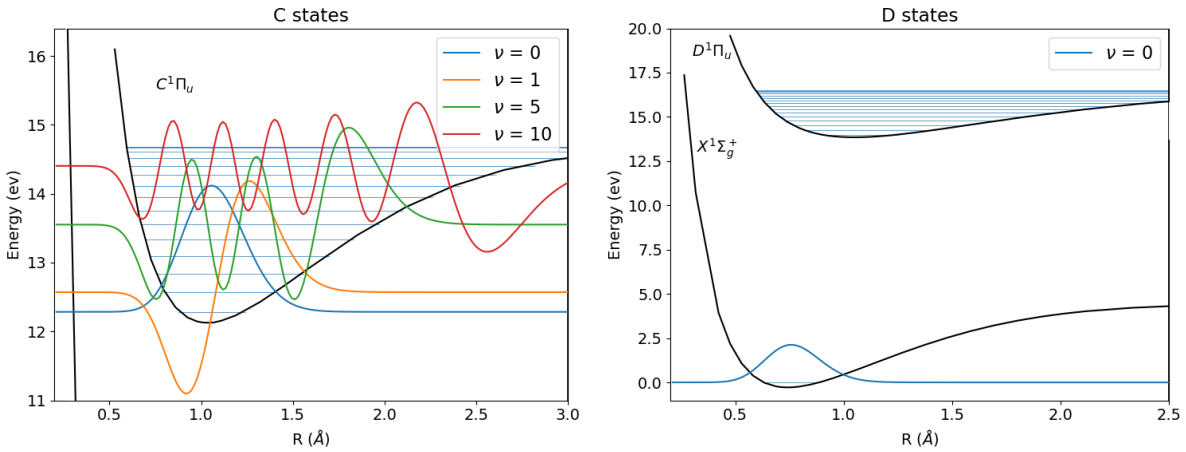

Figure 9: Graphical representation of the results given by *nucfix*. On the left, the first bound levels for the ground and the $C^1\Pi_u$ (C) potential curves are to see, as well as the nuclear wave function for some of them; on the right, the bound energy levels of the $D^1\Pi_u$ (D) states are presented.

Using the results obtained in *nucfix*, the code *rovib_trans* calculates the transition probabilities between the energy levels. Let $\hat{W}$ be the transition operator. The transition matrix element from an initial state to a final one is given by

$$T_{i\to f} = \langle \Psi_f(\boldsymbol{r},\boldsymbol{R})|\, \hat{W}\, |\Psi_i(\boldsymbol{r},\boldsymbol{R})\rangle \approx \langle \Psi_f(\boldsymbol{r},\boldsymbol{R})|\, \hat{d}\, |\Psi_i(\boldsymbol{r},\boldsymbol{R})\rangle \equiv d_{i\to f}, \tag{41}$$

where the dipole approximation was applied, meaning that the transition operator corresponds in first order to the dipole operator, $\hat{d}$. The transition probability between two states is given by the square of the matrix element,

$$P_{i\to f} = |T_{i\to f}|^2 \approx \left|\langle \Psi_f(\boldsymbol{r},\boldsymbol{R})|\, \hat{d}\, |\Psi_i(\boldsymbol{r},\boldsymbol{R})\rangle\right|^2. \tag{42}$$

Note, that the transition probability is calculated with the *total* wave function $\Psi(\boldsymbol{r},\boldsymbol{R})$. Inserting the Born-Oppenheimer approximation for the wave function, one arrives at

$$d_{i\to f} = \langle\psi_f(\boldsymbol{R})|\,\langle\phi_f(\boldsymbol{r})|\,\hat{d}\,|\phi_i(\boldsymbol{r})\rangle\,|\psi_i(\boldsymbol{R})\rangle\,, \tag{43}$$

where the central part of the inner product $\langle\phi_f(\boldsymbol{r})|\,\hat{d}\,|\phi_i(\boldsymbol{r})\rangle \equiv C_{if}$ is called the *couplings*. In this first integration, the dependency on $\boldsymbol{r}$ is removed, but the coupling is in general an $\boldsymbol{R}$-dependent quantity. Note, however, that *nucfix* only provides the *nuclear wave functions*. Therefore, the calculation of the couplings, which made used of the electronic wave functions, was not directly doable. Possible ways of addressing this problem are now presented.

One first option for getting around the calculation of the electronic wave functions is the use of the Frack-Condon approximation. This assumes that the couplings are completely independent of $\boldsymbol{R}$ and can be then taken out of the integration, as in the following equation

$$d_{i\to f} = \langle\phi_f(\boldsymbol{r})|\,\hat{d}\,|\phi_i(\boldsymbol{r})\rangle\,\langle\psi_f(\boldsymbol{R})|\psi_i(\boldsymbol{R})\rangle = C_{if}\,\langle\psi_f(\boldsymbol{R})|\psi_i(\boldsymbol{R})\rangle\,. \tag{44}$$

This approximation consists in estimating the transition probability as the overlap between the nuclear wave functions of the involved levels, which is called the Franck-Condon factor. The Franck-Condon approximation is, in general, a good approximation for the studied energy levels, since the excitation process involves vertical transitions, and it was done at the beginning of the project. Later on, an improvement of the calculation of the transition probabilities was implemented by including the dependency on $\boldsymbol{R}$ of the couplings, as shown in equation (45). The values of the couplings were obtained from literature [34, 35], such that

$$d_{i\to f} = \langle\psi_f(\boldsymbol{R})|\,C_{ij}(\boldsymbol{R})\,|\psi_i(\boldsymbol{R})\rangle\,. \tag{45}$$

The result was not substantially different, but the transition probabilities from the ground state to the excited states were slightly corrected, as it is shown for some potential curves in fig.10. In the following, the presented results will make use of the $\boldsymbol{R}$ dependent electronic couplings.

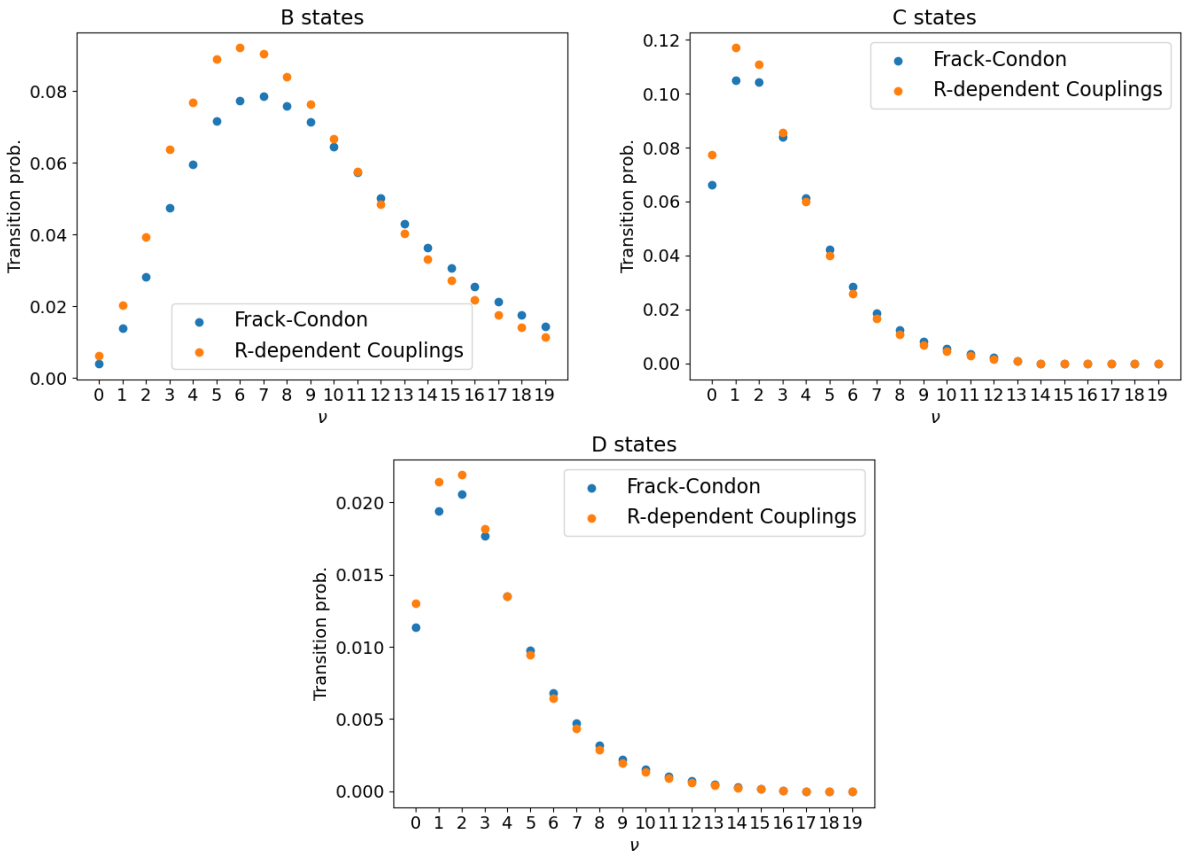

Figure 10: Comparison of the transition probabilities from the ground state when using the coupling elements in the Franck-Condon approximation and when including their R dependency for the B, C and D states. As it can be seen, the R-dependency introduces a small correction, and therefore, the corrected results are used in the following.

4.2 Model simulation of the experiment

Once the nuclear wave functions and the elements of the transition matrix between the energy levels were calculated, the simulation of the experiment presented in section 2 could be performed by implementing a multi level simulation.

4.2.1 Laser pulses

As mentioned in the experimental motivation section, the target is illuminated with two laser pulses, one XUV pulse, coming at $t = 0$ and one NIR pulse, coming at $t = \tau$, where τ is the *time delay*, and can be positive or negative, as the two configurations shown in fig.11. In this work, the transient coupling scheme will be the most relevant, but some results will also be presented for negative time delay.

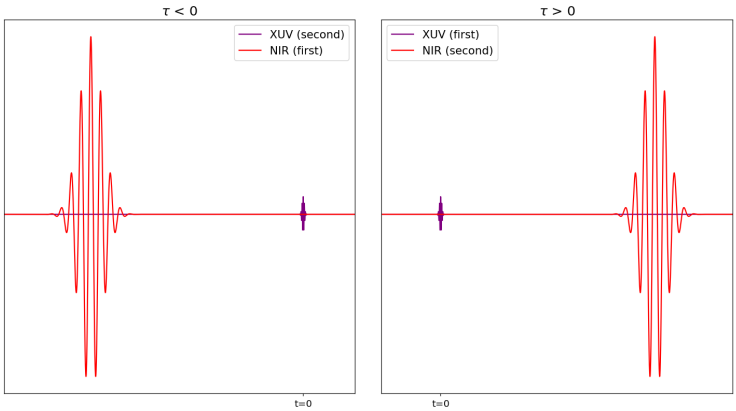

Figure 11: Possible laser configurations depending on the relative time delay between the NIR and XUV pulses. a)NIR arrives to the target earlier in time, in comparison to the XUV pulse. b)The XUV pulse interacts with the target at $t = 0$ and at a later time $t = \tau$, the NIR pulse arrives.

The most relevant parameters of the laser pulses that were used in the simulation are summarized in table 4. For the XUV energy, the value of 14 eV is chosen, since it is centred in the middle of the considered energy range, and the duration is chosen to cover the energy range. For the NIR energy, the duration (less than 5 fs) was characterized in a D-Scan setup before and after the experiment, and conservative 5 fs taken into account. The photon energy is selected to allow the transitions between the D- and the EF-bound states.

Table 4: Laser parameters. The energy and the shape of the pulses were kept constant for all sections of this work. However, a time delay scan was realized, so this parameter varies in the different sections.

XUV	NIR
FWHM = 0.5fs	FWHM = 5fs
E = 14eV	E = 1.6eV
t = 0	t = τ

Using these parameters, the two Gaussian pulses in the simulation were generated as two functions on a time grid, which represents the electric field for each t. In the following section, the Hamiltonian of the system is presented, with its interaction part directly depending on the presence of the laser electric fields.

4.2.2 Hamiltonian of the model system

The Hamiltonian of the system can be expressed as the sum of the free Hamiltonian $\mathcal{H}_0$ and the interaction Hamiltonian, $\mathcal{H}_{int}(t)$, which is time dependent.

$$\mathcal{H}(t) = \overbrace{\mathcal{H}_0}^{\substack{\text{atomic energies}\\ \text{(diag.)}}} + \overbrace{\mathcal{H}_{\text{int}}(t)}^{\substack{\text{laser interaction}\\ \text{(not diag.)}}} \tag{46}$$

The free Hamiltonian can be represented, in the eigenstate basis, as a diagonal matrix, which elements are the energy levels of the different electronic vibrational levels. The notation used for the energy of a particular level would be E_{curve_ν}, where ν is the vibrational quantum number. The considered curves are represented only by the letter, but their name would be completed with the full expressions written in equation (23).

The interaction Hamiltonian, $\mathcal{H}_{\text{int}}(t)$ introduces the non-diagonal terms responsible for the transitions between the levels. It can itself be divided into the interactions coming from the XUV and NIR pulses.

$$\mathcal{H}_{\text{int}} = \mathcal{H}_{\text{int, XUV}} + \mathcal{H}_{\text{int, NIR}} \tag{47}$$

These two laser pulses allow two types of states to be accessed. The so-called *bright states* (B, C and D) are allowed transitions from the ground X state. As it can be seen in fig.12 (example for the D state), the XUV pulse can provide the necessary energy for these transitions.

The *dark states* (EF states, in our case) however cannot directly be accessed from the ground state, due to the symmetry reasons explained above. The transition matrix elements between ground and EF states are 0. They can however be accessed from the bright states by interaction with the NIR pulse, as it is also shown in fig.12.

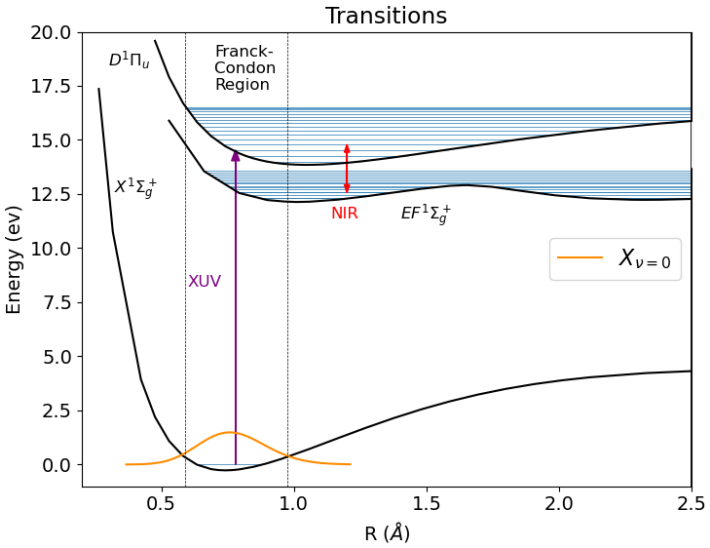

Figure 12: Example of some of the previously mentioned allowed transitions. This scheme with the X, D and EF levels is the one considered more often in the present work, and therefore chosen for the clarification. The simulation starts with all the population in the ground state. By illuminating the target with the XUV light, the bright states (in this case, the D states) can be accessed. The NIR causes the population transfer to the EF states. The most population is transferred from the ground state to the $D_{\nu=2}$, as it can be seen in the transition probabilities from fig.10.

In general, the interaction Hamiltonian for dipole transitions it is defined as the product of the dipole elements (obtained in equation (45)) with the electric field $\mathcal{E}(t)$ relevant for the transition,

$$\mathcal{H}_{\text{int},ij} = d_{i\to j}\mathcal{E}(t). \tag{48}$$

Therefore, the interaction Hamiltonian will have entries between transitions X $\to$ B, C, D, but the entries vanish for transitions X $\to$ EF, as shown in equation (25). However, the elements $B, C, D \to EF$ are also, in general, non-zero. The transitions from the ground state will be multiplied by the XUV electric field, $\mathcal{E}_{XUV}(t) \equiv \mathcal{E}(t)$, and the transitions from bright to dark states will depend on the NIR electric field $\mathcal{E}_{NIR}(t) \equiv \mathcal{E}(t)$.

In equation (50), an example of a constructed Hamiltonian for the system is represented. In this case, which is the case considered in most of the sections presented in chapter 5, the simulation includes the following levels:

1. The ground $X^1\Sigma_g^+(\nu = 0)$ state.
2. The 18 bound D states.
3. The 34 bound EF states.

Note, for clarity, the following colour code was used: blue for the diagonal elements of the free Hamiltonian, violet for the XUV transitions included in $H_{\text{int},XUV}$ and red for the NIR-mediated transitions, which come from $H_{\text{int},NIR}$. The non-allowed transitions correspond to zeros in the corresponding interaction Hamiltonian matrix elements. The total Hamiltonian is given by

$$\mathcal{H}(t) = \mathcal{H}_0 + \mathcal{H}_{\text{int, XUV}} + \mathcal{H}_{\text{int, NIR}}, \tag{49}$$

which when expanding its elements corresponds to

$$\mathcal{H}(t) = \begin{pmatrix} E_{X_0} & d_{XD_0}\mathcal{E}(t) & d_{XD_1}\mathcal{E}(t) & \cdots & 0 & 0 & \cdots & \cdots & 0 \\ d_{XD_0}\mathcal{E}(t) & E_{D_0} & 0 & \cdots & d_{D_0EF_0}\mathcal{E}(t) & d_{D_0EF_1}\mathcal{E}(t) & \cdots & \cdots & \cdots \\ d_{XD_1}\mathcal{E}(t) & 0 & E_{D_1} & \cdots & d_{D_1EF_0}\mathcal{E}(t) & d_{D_1EF_1}\mathcal{E}(t) & \cdots & \cdots & \cdots \\ \vdots & \vdots & \vdots & \ddots & \vdots & \vdots & \vdots & \vdots & \vdots \\ 0 & d_{D_0EF_0}\mathcal{E}(t) & d_{D_1EF_0}\mathcal{E}(t) & \cdots & E_{EF_0} & 0 & \cdots & \cdots & 0 \\ 0 & d_{D_0EF_1}\mathcal{E}(t) & d_{D_1EF_1}\mathcal{E}(t) & \cdots & 0 & E_{EF_1} & 0 & \cdots & 0 \\ \vdots & \vdots & \vdots & \vdots & \vdots & \vdots & \ddots & \vdots & \vdots \\ 0 & d_{D_0EF_{34}}\mathcal{E}(t) & d_{D_1EF_{34}}\mathcal{E}(t) & \cdots & 0 & 0 & 0 & \cdots & E_{EF_{34}} \end{pmatrix} \tag{50}$$

where the subindex of the states refers to the ν, but the full notation with the Greek letter is omitted to save space.

The simulation should also include the lifetime of the states. In order to do so, one possibility is to include an imaginary term in the free Hamiltonian energies. In the exponential solution from the time-dependent Schrödinger Equation, which will be shown in details in the next section, this imaginary term transforms into an exponential decay of the population. For a lifetime of $\frac{1}{\Gamma}$, the corresponding transformation is

$$E \leftarrow E - i\frac{\Gamma}{2}. \tag{51}$$

The selected decay rate Γ will be different for different parts of the analysis, so the used values will be later indicated. The ground state $X_{\nu=0}$ has no decay rate, since it would be unphysical that it decays into another state.

4.2.3 Solving the time-dependent Schrödinger Equation

In this section, the implementation of the solution of the time-dependent Schrödinger equation is derived, following the work done by [36].

The goal of the multi-level simulation is to numerically solve the time-dependent Schrödinger Equation for the wavefunctions, which in atomic units reads

$$\mathcal{H}(t)\,|\Psi(t)\rangle = i\frac{\partial}{\partial t}\,|\Psi(t)\rangle\,. \tag{52}$$

In order to solve it, a basis decomposition of the state vector $|\Psi(t)\rangle$ was done. The chosen basis is the free basis $\{|\,i\,\rangle\}_{i=1}^{N}$, where N is the total number of considered states, which are the eigenvectors of the free Hamiltonian $\mathcal{H}_0$, meaning

$$\mathcal{H}_0\,|\,i\,\rangle = E_{0,i}\,|\,i\,\rangle\,. \tag{53}$$

where $E_{0,i}$ is the energy of the molecular level. Therefore, it can be expressed as

$$|\Psi(t)\rangle = \sum_{i=0}^{N} c_i(t)\,|\,i\,\rangle\,. \tag{54}$$

The $c_i(t)$ elements correspond therefore to the population coefficients, and its square represents the probability of the system to be in a given state, i. The basis of the nuclear states, $\{|\,i\,\rangle\}_{i=1}^{N}$ is known from the *nucfix* results. One therefore must solve for the state vector $\vec{c}(t)$, defined as

$$\vec{c}(t) = \begin{pmatrix} c_0(t) \\ c_1(t) \\ \vdots \\ c_N(t) \end{pmatrix}. \tag{55}$$

Solving equation (52) gives an exponential solution for the state vector, meaning, in atomic units,

$$\vec{c}(t) = e^{-i\mathcal{H}(t)\cdot t}\,\vec{c}(0), \tag{56}$$

where $\vec{c}(0)$ represents the state vector at $t = 0$. In the simulation, the system always starts with the total population in the ground state, which means that

$$\vec{c}(0) = \begin{pmatrix} 1 \\ 0 \\ \vdots \\ 0 \end{pmatrix}. \tag{57}$$

The solution of the TDSE is then the evolution of the system for a total lapse of time T divided in steps Δt, such that if $t_n = t_0 + n\Delta t$ for n an integer number, one has, according to equation

$$\vec{c}(t_n) \leftarrow e^{-i\mathcal{H}(t_{n-1})\cdot\Delta t}\, \vec{c}(t_{n-1}), \tag{58}$$

or equivalently

$$|\Psi(t_n)\rangle \leftarrow e^{-i\mathcal{H}(t_{n-1})\cdot\Delta t}\, |\Psi(t_{n-1})\rangle\,. \tag{59}$$

The diagonalization of the Hamiltonian is then required at each time step. However, calculating it for the full matrix at each time step would be computationally very expensive. Therefore, an approximation was done, by which to a second order precision the time propagation can be decomposed in (see [17] for more details)

$$e^{-i\mathcal{H}(t)\cdot t} = e^{-i(\mathcal{H}_0+\mathcal{H}_{\text{int}}(t))\cdot t} \approx e^{-i\mathcal{H}_0\cdot\frac{t}{2}}\, e^{-i\mathcal{H}_{\text{int}}(t)\cdot t}\, e^{-i\mathcal{H}_0\cdot\frac{t}{2}}. \tag{60}$$

This solves part of the problem. Inserting the decomposition in equation (59), and since the basis elements are eigenvalues of $\mathcal{H}_0$, the exponential part $e^{-i\mathcal{H}_0\cdot\frac{t}{2}}$ is also a diagonal matrix, and one can directly apply

$$|\Psi(t_n)\rangle \leftarrow e^{-i\mathcal{H}_0\cdot\frac{t}{2}}\, e^{-i\mathcal{H}_{\text{int}}(t)\cdot t}\, e^{-i\mathcal{H}_0\cdot\frac{t}{2}}\, |\Psi(t_{n-1})\rangle\,, \tag{61}$$

where the application of the half-time evolution of the free hamiltonian to the state vector $e^{-i\mathcal{H}_0\cdot\frac{\Delta t}{2}}\, |\Psi(t_{n-1})\rangle$ is equivalent to the multiplication of each of the coefficients by its free energy evolution $e^{-iE_{0,i}\cdot\frac{\Delta t}{2}} c_i(t_{n-1})$.

However, the diagonalization of the interaction Hamiltonian is still required. Again, an approximation will be applied, which states that

$$e^{-i\mathcal{H}_{\text{int}}(t)\cdot t} = e^{-i\left(\mathcal{H}_{\text{int},XUV}(t)+\mathcal{H}_{\text{int},NIR}(t)\right)\cdot t} \approx e^{-i\mathcal{H}_{\text{int},XUV}(t)\cdot t}\, e^{-i\mathcal{H}_{\text{int},NIR}(t)\cdot t}. \tag{62}$$

Therefore, the interaction Hamiltonian for the XUV and NIR lasers can be propagated

independently. This implies a great simplification, because the electric field can then be factored out of each of the matrices, and the unitary eigenvectors of $\mathcal{H}_{\text{int,XUV}}$ and $\mathcal{H}_{\text{int,NIR}}$ remain constant in time. Note that the eigenvalues do depend on the electric field, but just as a multiplicative factor. The basis change is then calculated

$$\mathcal{H}^D_{\text{int,XUV}}(t) = T^{-1}_{\text{XUV}} \mathcal{H}_{\text{int,XUV}}(t) T_{\text{XUV}}, \tag{63}$$

$$\mathcal{H}^D_{\text{int,NIR}}(t) = T^{-1}_{\text{NIR}} \mathcal{H}_{\text{int,NIR}}(t) T_{\text{NIR}}, \tag{64}$$

where the matrixes T_{XUV} and T_{NIR} are time independent. The diagonalization must be carried out just once, at the beginning of the simulation.

Applying now the time evolution induced from the interaction Hamiltonian and decomposed as in equation (62), the basis change is first applied to the $\mathcal{H}_{\text{int,XUV}}$ basis to the state, as

$$\left|\Psi^D_{XUV}(t)\right\rangle = T^{-1}_{\text{XUV}} \left|\Psi(t)\right\rangle. \tag{65}$$

Next, the time evolution is applied, where note that, as in the case of the free evolution, now the exponential operator is also a diagonal matrix, which multiplies the states

$$\left|\Psi^D_{XUV}(t_n)\right\rangle \leftarrow e^{-i\mathcal{H}^D_{\text{int,XUV}}(t_{n-1})\cdot\Delta t} \left|\Psi^D_{XUV}(t_{n-1})\right\rangle. \tag{66}$$

Lastly, one must return to the original free Hamiltonian basis, which is achieved by the transformation

$$\left|\Psi(t)\right\rangle = T_{\text{XUV}} \left|\Psi^D_{XUV}(t)\right\rangle. \tag{67}$$

The whole process is repeated, now with a basis change to the $\mathcal{H}_{\text{int,NIR}}$ basis, as follows

$$\left|\Psi^D_{NIR}(t)\right\rangle = T^{-1}_{\text{NIR}} \left|\Psi(t)\right\rangle. \tag{68}$$

The time evolution has now the form

$$\left|\Psi^D_{NIR}(t_n)\right\rangle \leftarrow e^{-i\mathcal{H}^D_{\text{int,NIR}}(t_{n-1})\cdot\Delta t} \left|\Psi^D_{NIR}(t_{n-1})\right\rangle. \tag{69}$$

and lastly one returns to the original basis by transforming back the state

$$|\Psi(t)\rangle = T_{\text{NIR}} \left|\Psi^D_{NIR}(t)\right\rangle . \tag{70}$$

Following equation (60), the second half of the free-Hamiltonian time evolution must be applied, that means, the state vector must once more be multiplied with the exponential of $\mathcal{H}_0$

$$|\Psi(t_n)\rangle \leftarrow e^{-i\mathcal{H}_0 \cdot \frac{\Delta t}{2}} |\Psi(t_{n-1})\rangle . \tag{71}$$

Summarizing, the whole time evolution for each time step can be represented as

$$|\Psi(t_n)\rangle = e^{-i\mathcal{H}_0 \cdot \frac{\Delta t}{2}} T_{\text{NIR}}\, e^{-i\mathcal{H}^D_{\text{int,NIR}}(t_{n-1})\cdot \Delta t}\, T^{-1}_{\text{NIR}}\, T_{\text{XUV}}\, e^{-i\mathcal{H}^D_{\text{int,XUV}}(t_{n-1})\cdot \Delta t}\, T^{-1}_{\text{XUV}}\, e^{-i\mathcal{H}_0 \cdot \frac{\Delta t}{2}} |\Psi(t_{n-1})\rangle . \tag{72}$$

4.2.4 Relevant quantities: the time-dependent dipole moment and the Optical Density

In addition to the state vector, the Time-Dependent Dipole Moment (TDDM) was computed at every time step. The TDDM with respect to the ground state is defined as follows

$$d(t) = \langle \Psi(t)| \hat{\mathbf{d}} |\Psi(t)\rangle = \sum_{i=1}^{N} c_0^*(t) c_i \langle 0 | \hat{\mathbf{d}} | i \rangle + c.c. \tag{73}$$

By using the time-dependent dipole moment, the cross-section can be calculated as expressed in equation (12). From it, the optical density can also be calculated, following equation (13).

The time-dependent dipole moment and the optical density are the two most relevant experimental quantities that were compared with the simulation. In the following section, the results obtained from the multi-level simulation will be presented.

5 Results

In this chapter, the previously explained concepts and simulation schemes will be applied to model the hydrogen molecule under the influence of external fields and compare the simulated results to the experimental data. Several aspects of the population transition process are evaluated, including the creation of a nuclear wavepacket and its time evolution, the time-dependent dipole moment and the absorption lines from the optical density. The following subsections deliver details for each of those calculations.

In this part, the main focus is on the transition scheme represented in fig.13. Only the ground state, the 18 D-bound states and the 35 EF-bound states are included in the calculation. As a starting point, all the molecules can be found in the ground state. By means of the interaction with the XUV field, part of the ground-state population is excited and transferred to the D states. After a time delay τ, the NIR pulse hits the target, and creates a population transfer between the D and the EF states. The Hamiltonian of the system is exactly the one given in equation (50), but including the mentioned decay rate, with a value of $\Gamma = 1e^{-4}$ a.u.. (Of course, the ground level has no decay). Except for the section on configuration interaction, where some continuum level will also be included, these will be the levels included in the model system.

5.1 The nuclear wavepacket

One calculation of particular interest from the simulations is the construction of a nuclear wavepacket, since it cannot directly be accessed from the experimental data. In our case, the focus is on the wavepacket consisting of the superposition of the D eigenstates, since those energy levels correspond to the most visible lines in the experimental results.

Let $\{|\Psi_i\rangle\}_{i=0}^{17}$ be the eigenvectors of the free Hamiltonian corresponding to the D-states (meaning $\{|\Psi_i\rangle\} \in \{|\, i \,\rangle\}$). One can construct the corresponding wavepacket as

$$|\Psi_D(t)\rangle = \sum_{i=0}^{17} c_i(t)\, |\Psi_i\rangle\,. \tag{74}$$

Note that the square of the $c_i(t)$ coefficients correspond to the population fraction that can be found at a given energetic level. Therefore, at $t = 0$, these coefficients correspond to the transition probabilities from the ground state to the D state, obtained from the *rovib_trans* code. Using the results of fig.10, the wavepacket at $t = 0$, as represented in fig.13, is obtained.

In this picture, the Franck-Condon region was represented, which is defined as the region of the final potential energy surface which is accessed by the vertical transition from the initial state. Note that the wavepacket at $t = 0$ basically looks like a copy of the original

ground state wave function, since indeed the coupling elements just calculate the fraction of overlap of each excited level with the ground state. Outside the Franck-Condon region, the XUV transition is very unlikely, since there is almost no overlap between the nuclear wavefunctions of the involved levels.

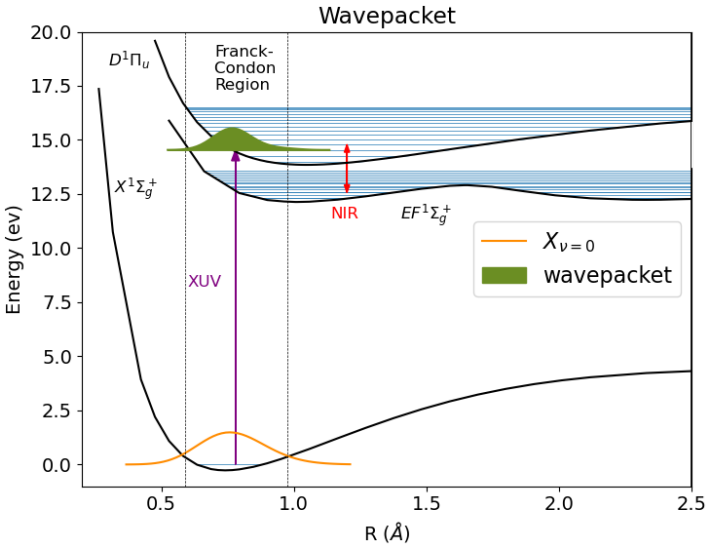

Figure 13: Scheme of the energetic levels involved in the simulation. The ground state, the 18 D-bound states and the 34 EF-bound states are included in the calculation. Using the transition probabilities from the ground to the excited states as obtained from *nucfix*, the wavepacket of the D states at $t = 0$ could be obtained, which is represented in green in the picture. The Franck-Condon region is also marked.

By using the simulation to model the time evolution, as explained in section 4, one could calculate the state vector defined in equation (55) for every time step. Making use of these coefficients, one could obtain the wavepacket at each time step, as given in equation (74). The result of this calculation can be seen in fig.14, in this case, for time delay $\tau = 7$.

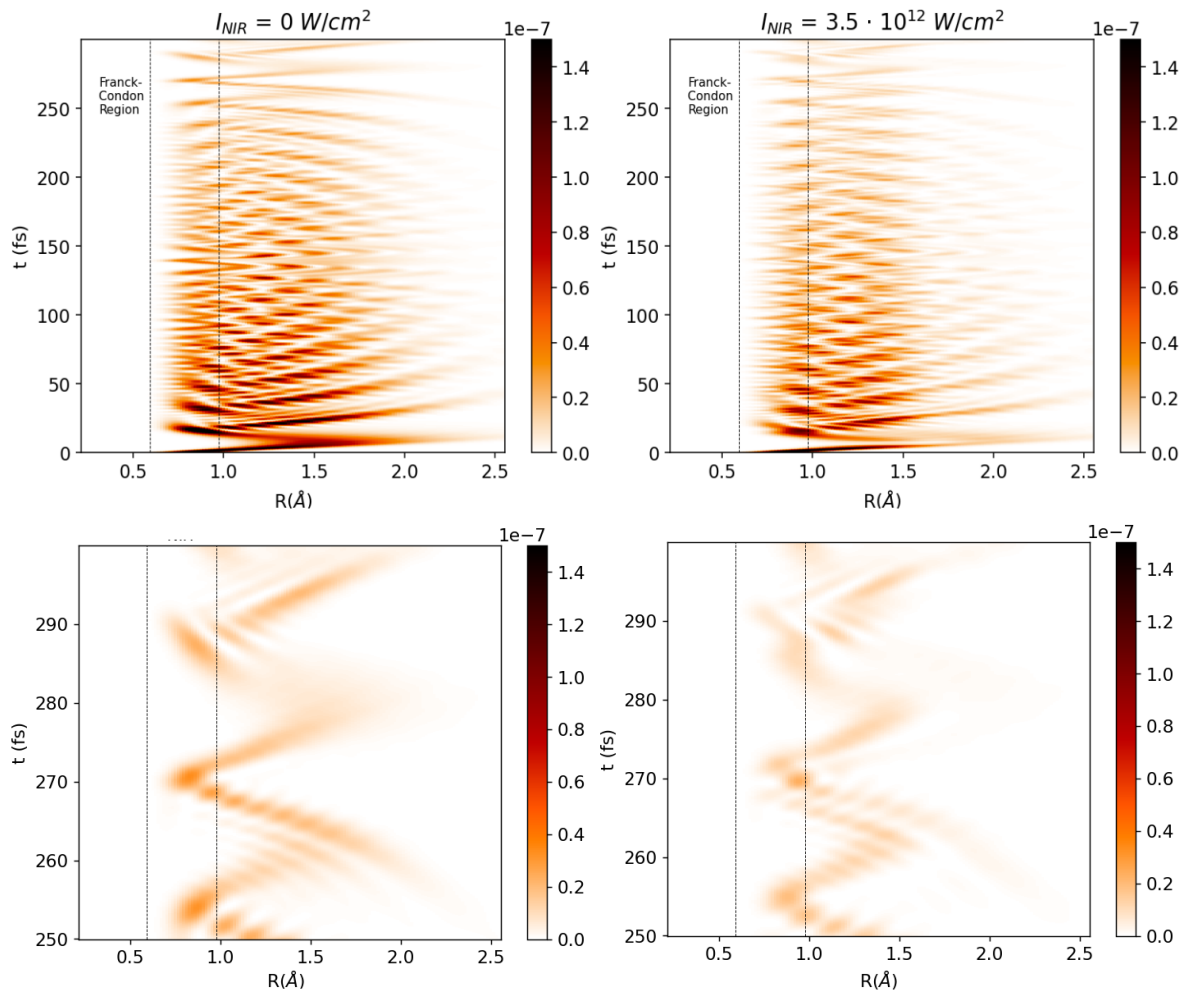

Figure 14: Time evolution of the D-states wavepacket. On top, one can see a longer time range for no NIR light (left) and for a middle-to-strong intensity (right) of the NIR field, which has a time delay of $\tau = 7\,\text{fs}$. Below, the zoomed versions around the revival time ($t \sim 172\,\text{fs}$). The Franck-Condon region is also displayed in the figure.

As shown in fig.14, the wavepacket moves in space and time. If one compares the two intensities at time $t = \tau = 7\,\text{fs}$, one can appreciate a distortion in the one including the NIR field, indicating that the pulse kicks at this moment.

As expected from a time-evolving wavepacket, its components get out of phase with time, and the nice and clear Gaussian shape that could be observed at the beginning of the time evolution gets distorted. According to theory, however, a revival of the wavepacket when the components get again in phase is expected to happen at around $t \sim 272\,\text{fs}$ (see zoomed pictures). One can indeed observe a nice revival in the case of the non-distorted by the NIR wavepacket. When some NIR interacts with the target, it adds an additional phase to the time evolution, which distorts the wavepacket revival, as it can be seen in the case including the NIR. In the next section, further comments on this distortion, and other interesting effects on the revival time created by the NIR field, will be presented.

5.2 The wave-packet revival time

The next observable to be studied was the time-dependent dipole moment (TDDM), computed as presented in section 4.2.4. This quantity can also be obtained from the experimental data measured by Gergana D. Borisova. In that case, the OD is measured, and the time-dependent dipole moment is reconstructed from the experimentally measured absorption spectra by Fourier transforming and invoking causality. More details on this procedure can be found in [37]. On the contrary for the simulation, and as explained in the theory section, the time-dependent dipole moment was calculated at each time step, and the OD is proportional to its Fourier transform, as expressed in equation (13).

The experimental and simulated results for the time-dependent dipole moment are plotted in fig.15. The evaluation of the experimental of the data is not part of this project, just the results are stated here. Recalling equation (73), the time-dependent dipole moment can be seen as a measure of the overlap between the D-states wavepacket with the original ground state. As expected, it has clear oscillations for earlier times (0-20fs), when the wavepacket still preserves the Gaussian form, and it loses regularity, as the components of the wavepacket go out of phase and the defined wavepacket disappears. These earlier-time oscillations are not to be seen in the experiment, due to the technique used to obtain the TDDM from the experimental data.

The revival of the wavepacket is also visible in the TDDM at around $t \sim 272\,\mathrm{fs}$, as previously observed in the plots of the wavepacket's time evolution. At this moment, the wavepacket recovers its form and has a significant overlap with the ground state when travelling through the Franck-Condon region. In the picture, these spatial oscillations of the wavepacket can again be clearly seen in the region between the two vertical black lines, as also clear oscillations of the TDDM.

Interestingly, the time of the revival seems to be shifted to an earlier moment with increasing the intensity of the NIR field. This is due to the additional phase added by the interaction with the NIR light to the free time evolution of the states. If a given state i has a coefficient $c_i(t)$ which evolves as (see equation (56))

$$c_i(t) = c_i(0)e^{-iE_i \cdot t}, \tag{75}$$

then, the NIR light changes the amplitude and adds an additional phase, which can be expressed as

$$c_i(t) = c_i(0)e^{-iE_i \cdot t}a_i e^{-i\Delta\phi_i}, \tag{76}$$

where a_i would be the factor indicating the change in amplitude and $\Delta\phi_i$, the additional

phase.

Intuitively, one could say that this extra phase accelerates the process of the D-states getting again in phase and causes the shifting of the revival to an earlier time. More on the effects of the phase change caused from the NIR interaction will be presented in section 5.5.

In fig.16, the Optical Density measured in the experiment and calculated in the simulation by using equation (13) is also shown. The agreement between experiment and simulation for the position of the lines indicates that the calibration of the energy position, on the one side, and the calculation of the energy levels and the nuclear wave functions, on the other, were accurate enough. However, the line shape of the resonance lines varies a lot between experiment and simulation. For example, if one looks at the lower NIR intensity case, the experimental lines have a Fano shape, while the simulated ones are Lorentzian. This problem will be addressed in the next section by the introduction of the configuration interaction, as a coupling to the continuum states, the D lines (starting from $D_{\nu=3}$) are embedded in. Notice also that the increasing of the NIR light reduces the definition of the revival, which has a two-bump shape. This feature will be analysed in section 5.5.

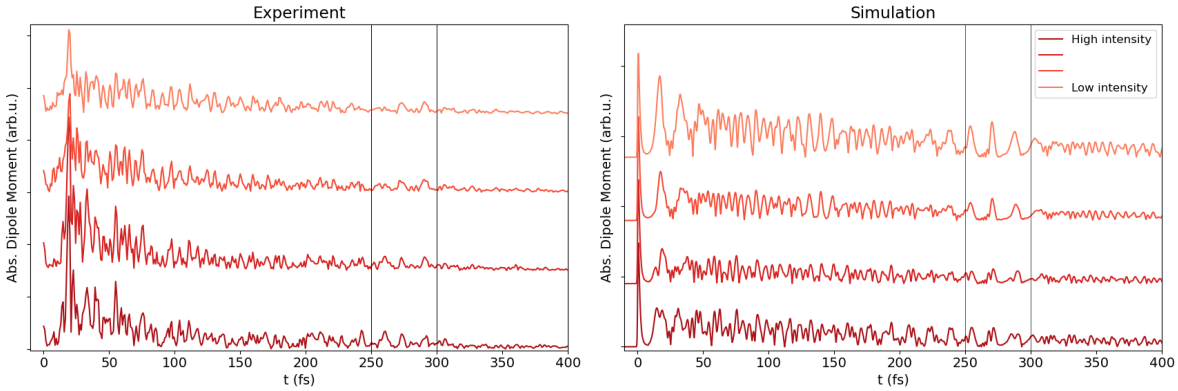

Figure 15: Time-dependent dipole moment from experiment and simulation for increasing (lighter to darker red) NIR Intensity. Due to the Fourier transform technique used to obtain the experimental TDDM, the first time steps are not as clear as in the simulation. The two vertical lines marked in both, experimental and simulated results, indicate the time when the revival of the wavepacket is expected to take place. Moreover, a small shift in the revival time with increasing NIR intensity can also be seen in both plots. One can also see how increasing of the NIR light reduces the definition of the revival.

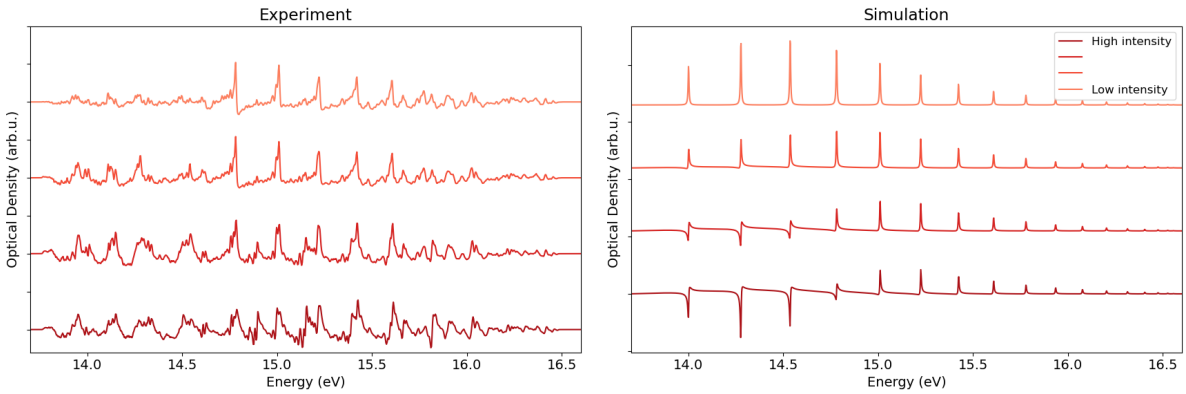

Figure 16: Optical Density from experiment and simulation for increasing (lighter to darker red) NIR Intensity. As it can be observed, the position of the lines agrees in both graphs. However, the line shapes differ greatly, even with sign inversions. This problem will be addressed in the following section.

Negative values for the optical density are valid for both, experiment and simulation. On the one hand, and as mentioned in section 3.2, the experiment calculates the pseudo-optical density, which uses a low-passed-filtered version of the signal as a reference. Therefore, negative values for equation (1) can be obtained. On the other hand, no general absorption procedure was included in the simulation. The only light-matter interaction which was included are the before mentioned near-to-resonance transitions. No continuum was included here. When no NIR photons are included in the simulation, the transitions are Lorentzian and the optical density only has positive values. However, the lines lose their symmetry when the molecules interact also with the NIR light, causing that in some energy positions, they could actually exceed the reference on one of the sides, which would result in negative values for the OD.

5.3 Treatment of the continuum in the model simulation

As mentioned in the previous section, when including only bound states in the model system, there was a disagreement in the line shape between experiment and simulation. According to Fano theory, the continuum levels need to be included in the simulation in order to get the Fano line shape observed in the experiment also in the case of no NIR light.

In order to improve the model, some continuum levels in the simulation are introduced and their interaction with the bound states via a time-independent configuration interaction is allowed, as explained in section 3.4. To demonstrate the effect, a toy-problem is first implemented, which included very few levels. Afterwards, the whole desired system is implemented. In the last part of this section, the problems of this approach are described, and an alternative approach to the continuum model based on additional phases is presented.

5.3.1 Few-level toy model

In order to demonstrate the effects of the configuration interaction, a very simple model is implemented, in which only the ground state, one bound D-state and one continuum state, considered to be one of the free states of the B potential curve, are included. The chosen states include the $D_{\nu=3}$ bound state, since it is the first state lying above the dissociation continuum and additionally the strongest resonance in the experimental data, and also a free B state degenerate in energy with the bound state. A sketch of this interaction system is presented in fig.17.

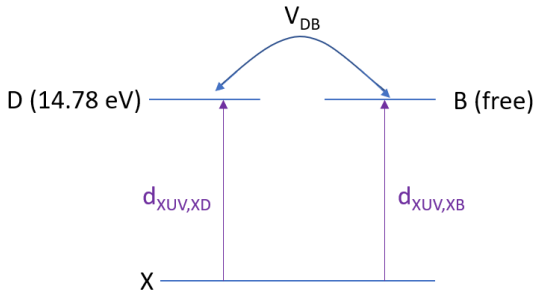

Figure 17: Sketch of the energy levels included in the toy model. It includes the ground state, the $D_{\nu=3}$ bound state and also a free B state degenerate in energy with the D state.

The corresponding Hamiltonian for such a system would include the configuration interaction elements, V_{DB}, in the non-diagonal elements describing the interaction between the B and the D lines, as follows

$$\mathcal{H}(t) = \begin{pmatrix} E_{X_0} & d_{XD_0}\mathcal{E}(t) & d_{XB_{cont}}\mathcal{E}(t) \\ d_{XD_0}\mathcal{E}(t) & E_{D_3} & V_{DB} \\ d_{XB_{cont}}\mathcal{E}(t) & V_{DB} & E_{B_{cont}} \end{pmatrix} \tag{77}$$

where the terms in green refer to the configuration interaction, the diagonal contains the free energies and again the dipole interaction matrix elements with the XUV light are represented in purple. Note that no EF levels are present in the simulation, therefore, no NIR-mediated interaction takes place.

The effect of the introduction of the configuration interaction is shown in fig.18, in the case of a relatively high V_{DB} value. At $t = 0$, part of the population (initially fully in the ground state) is transferred to both D and B states. Both of them are accessible from the ground state. However, the dipole-matrix element between the ground and the D states is bigger than the one between the ground and the B states, since the last one is a free state.

Therefore, the population is more likely to be transferred to the D state than to the B, as it can be observed in the figure.

Next, due to the configuration interaction, the population oscillates between the D and the B states, which are now coupled. This coupling is static in time. The decay of the states is due to the lifetime included in the simulation.

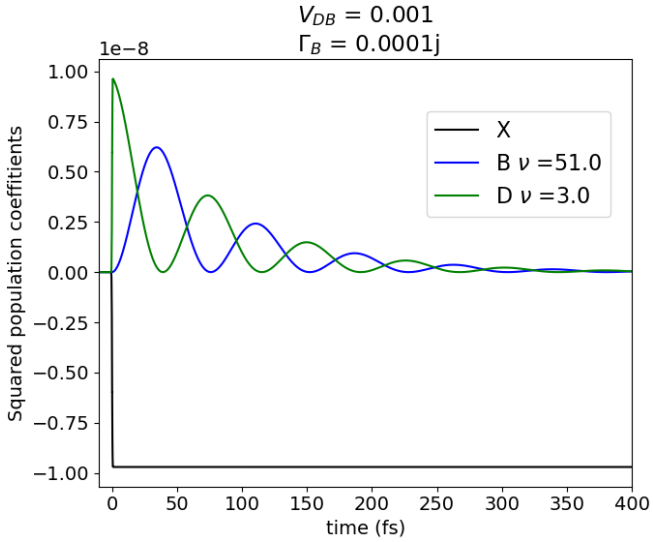

Figure 18: Population fraction evolution for the energy levels involved in the toy problem. The population fraction has a value between 0 and 1. Note, he unity was subtracted from the population of the ground state, to keep a readable scale for the plot. At $t = 0$, the XUV pulse interacts with the system and part of the population is transferred to the excited B and D states. The population oscillation between the two excited levels is caused by the static configuration interaction.

The absorption lines also change due to the introduction of the configuration interaction. As it can be seen in fig.19, the stronger configuration interaction causes that the lines start repelling each other. This effect is a consequence of the non-diagonal hamiltonian that the configuration interaction requires, which enforces a basis change. The eigenstates of the hamiltonian do not correspond to the theoretical energy lines any more. While an infinite number of states exist in nature, which repulsion effects can compensate, only one continuum line was implemented in this toy problem. Therefore, by this mean, the experimental results could not be recovered. Some work of fine-tuning with the interaction strength and sign was carried on with no satisfying results. Therefore, a different approach will be proposed at the end of this section.

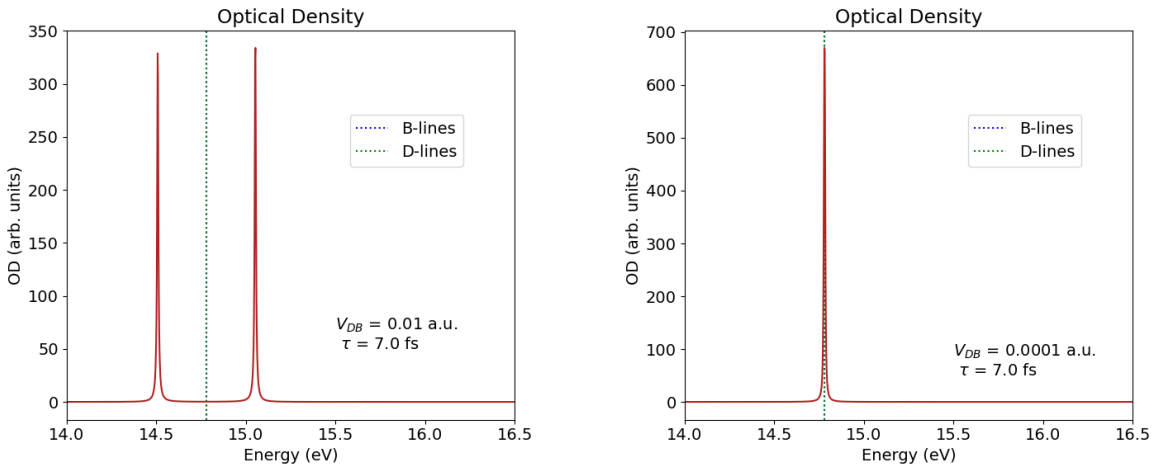

Figure 19: Optical density from the toy-problem simulation. In the figure on the left, a stronger configuration interaction is implemented, therefore, the repulsion between the lines is more pronounced and the B line is more present than in the figure on the right, with a weaker coupling. The lines were fit to Fano lines and a finite q-value estimate was obtained, however the change of the line shape is small and introduces an energy shift with respect to the experimental lines.

The NIR interaction is now added to the toy problem, by letting that the 35 bound states of the EF potential curve could be accessed through the NIR field. In fig.20, the population fraction for this case is plot. Again, the XUV field excites the system at $t = 0$. At $t = \tau = 7$fs, the NIR pulse transfers some population to the EF levels. In this case, the V_{DB} parameter was chosen a bit smaller ($V_{DB} = 10^{-3}$ a.u.), which is closer to the *rovib_trans* calculated values, and the population oscillations between D and B states are not that pronounced.

If one now takes a look to the simulated optical density for this case, the line shape is not Lorentzian any more. However, neither in this case it corresponds to the experimentally measured lines, which usually had first the positive peak and afterwards the negative valley. Moreover, the interaction with 35 energy levels includes too many variables and makes the fine-tuning very difficult. A different approach, which will be presented in section 5.3.3, is therefore discussed.

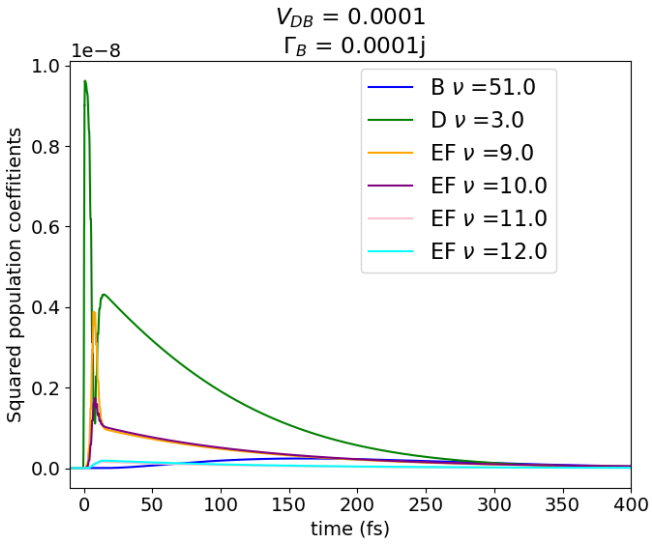

Figure 20: Population fraction evolution for the energy levels, including the EF bound states. The population fraction has a value between 0 and 1. At $t = 0$, the XUV pulse interacts with the system and part of the population is transferred to the excited B and D states. At $t = \tau = 7$fs, the NIR pulse arrives and allows the coupling to the EF states. The EF states with the highest coupling to the D states are the ones depicted for the illustration.

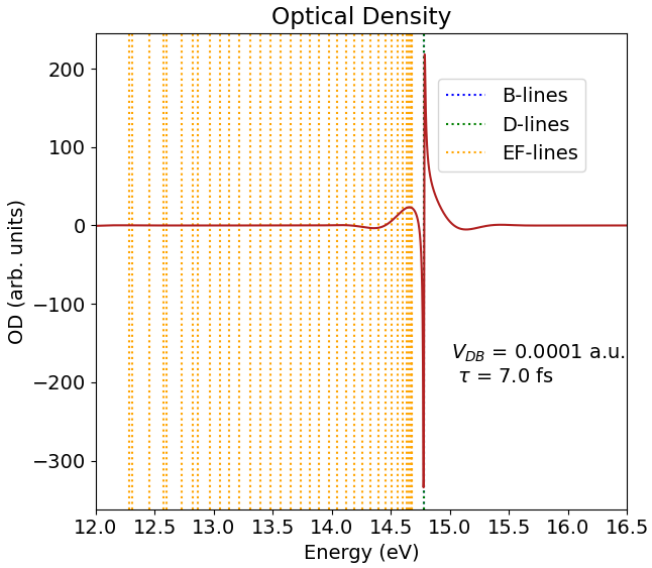

Figure 21: Optical density for the energy levels involved in the toy problem plus all the EF bound levels. The line is not Lorentzian any more, but it is still not fitting the experimental shape for this intensity. Moreover, in orange, it can be seen how many levels were needed to produce this line shape. This amount of simulation parameters is too big for fine-tuning.

5.3.2 Including all bound states

After considering the toy problem, the configuration interaction is introduced for a system including all the D and EF bound levels and one continuum state. The continuum state has now an energy of 17eV and a longer lifetime ($\Gamma_B = 2$ a.u.), in order to get a broad continuum line which would span in energy all the D bound-states energy levels. The result is plot in fig.22. All the lines present the energy shift, which does not correspond to the experimentally-measured results. The tuning of the V_{DB} parameter did not solve the problem. Therefore, a new approach for the problem was implemented, as it is described in the next section.

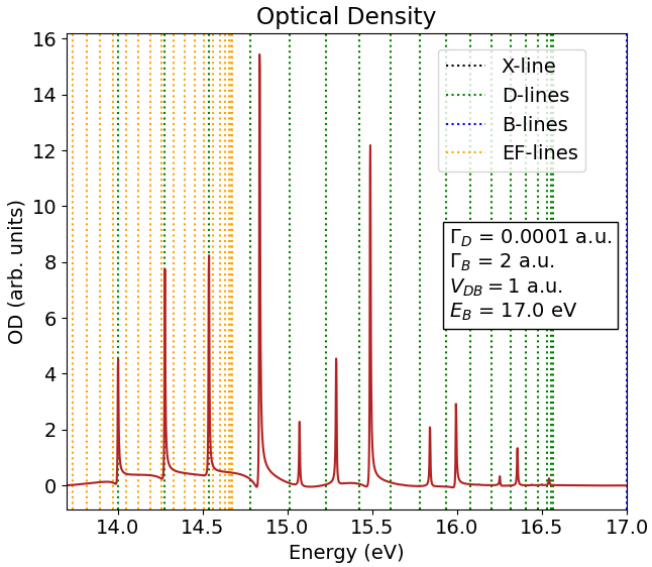

Figure 22: Simulated optical density when including all the EF and D bound levels. The energy shift that can be seen with respect to the expected line positions (dashed) is not matching the experimental results.

5.3.3 Fano phases

The introduction of the configuration interaction model described in the theory section leads to the desired Fano line shape for the simulation lines, needed for the results to agree with the experimentally measured lines. However, when implementing the configuration interaction, an energy shift in the energy of the lines appears. Mathematically, this is expressed in equation (36), where one can see that the parameter ϵ depends not on the energy E, but on the energy difference $E - E_\Phi$, being E_Φ the energy of the *modified* bound state. With increasing configuration interaction strength V_E, the shift of the lines becomes more and more pronounced. To proceed further with this approach, one must then shift the initial energy of the states, to make then the resonances appear on the right positions. This, however, includes a great fine-tuning work, which would become impossible when expanding further the model.

Here, a different formalism is introduced, in which the effects described by Fano can be achieved by adding an additional phase to the dipole moments. Here, the values for these phases, such that they match the definition of the q-parameter given in equation (38), are just stated. For a more formal description, previous papers of this group [10, 38, 39] are referred. The desired transformation includes the Fano Phase ϕ_F, which is related to the q value by

$$\phi_F = \arg(q - i), \tag{78}$$

and the desired transformation of the dipole moment is given by

$$d_{i\to f} \leftarrow d_{i\to f}\, e^{\phi_F i}. \tag{79}$$

With these changes, the Hamiltonian of the system, where all the bound levels for D and EF are included reads

$$\mathcal{H}(t) = \begin{pmatrix}
E_X & d_{XD_0}\mathcal{E}(t)e^{i\phi_F} & d_{XD_1}\mathcal{E}(t)e^{i\phi_F} & \cdots & 0 & 0 & \cdots & \cdots & \cdots \\
d_{XD_0}\mathcal{E}(t)e^{i\phi_F} & E_{D_0} & 0 & \cdots & d_{D_0EF_0}\mathcal{E}(t) & d_{D_0EF_1}\mathcal{E}(t) & \cdots & \cdots & \cdots \\
d_{XD_1}\mathcal{E}(t)e^{i\phi_F} & 0 & E_{D_1} & \cdots & d_{D_1EF_0}\mathcal{E}(t) & d_{D_1EF_1}\mathcal{E}(t) & \cdots & \cdots & \cdots \\
\vdots & \vdots & \vdots & \ddots & \vdots & \vdots & \vdots & \vdots & \vdots \\
0 & d_{D_0EF_0}\mathcal{E}(t) & d_{D_1EF_0}\mathcal{E}(t) & \cdots & E_{EF_0} & 0 & \cdots & \cdots & \cdots \\
0 & d_{D_0EF_1}\mathcal{E}(t) & d_{D_1EF_1}\mathcal{E}(t) & \cdots & 0 & E_{EF_1} & 0 & \cdots & \cdots \\
\vdots & \vdots & \vdots & \vdots & \vdots & \vdots & \ddots & \vdots & \vdots \\
0 & d_{D_0EF_{34}}\mathcal{E}(t) & d_{D_1EF_{34}}\mathcal{E}(t) & \cdots & 0 & 0 & 0 & \cdots & E_{EF_{34}}
\end{pmatrix}$$

Note, however, that for the first three energy states of the D-potential curve, the value $\phi_F = 0$ was selected. Physically, these lines are lower in energy than the dissociation energy of the B states, and therefore, they are technically not embedded in a continuum.

In order to get the desired shape, the experimental lines for the case of no NIR light are fitted to Fano lines, to obtain an estimate of the q parameter. A plot and more details about the fitting (fig.25) are presented in the following section, since to fit the experimental lines one needs to consider the experimental resolution. After getting the estimated value for the q parameter and implementing the transformation of the dipole elements as given in equation (79), the optical density and the time-dependent dipole moment are calculated.

In fig.23, the experimental and simulated optical densities are presented. The results for the line shape are in better agreement with the experiment. Of special relevance is the fact

that the fit of the experimental line shape to obtain the q-value is done only for the case of no NIR light. When increasing the NIR light, the Fano phase was kept the same, and still the lines are in good agreement, as long as they are visible in the experimental case.

In fig.24, the dipole moments are again compared between the experimental and the simulated results for completion. The revival is still observed and its shift due to the increasing NIR light is still noticeable.

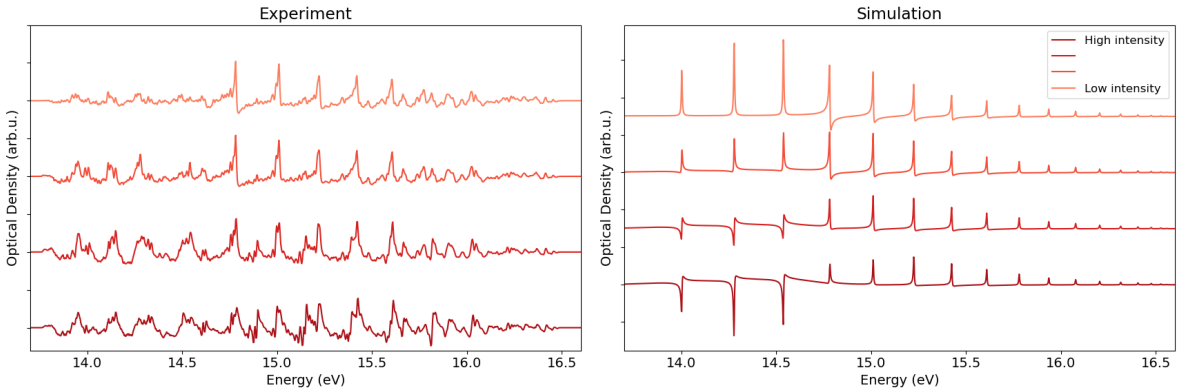

Figure 23: Optical Density from experiment and simulation for increasing (lighter to darker red) NIR Intensity and including the Fano phases in the dipole used in the simulation. Again, the position of the lines in both graphs is in great agreement. Moreover, the line shape is in agreement for the experimental and simulated results, thanks to the implementation of the Fano phases.

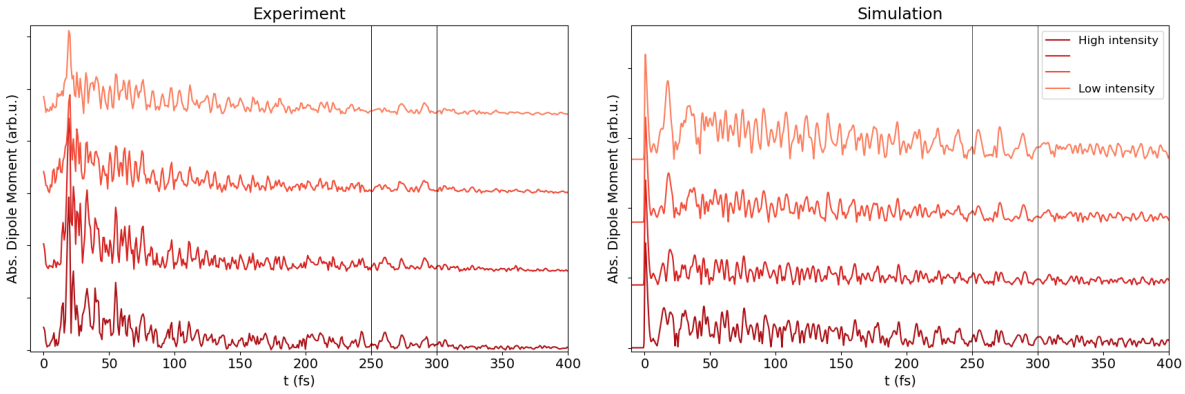

Figure 24: Time-dependent dipole moment for increasing (lighter to darker red) NIR Intensity when including the Fano phases. The revival is still observed. Moreover, the loose in the revival resolution is a bit more clear when introducing the Fano phases. This problem will be addressed in section 5.5.

Table 5: q values used in the simulation for the D-bound states. The first three energetic levels were chosen to have a large q value, to keep their Lorentzian shape. For levels $3 \leq \nu < 8$, the q values were obtained by fitting the experimental lines to Fano lines. For higher levels, the experimental lines could no longer be that well resolved, and the constant value of -9.3 used in [40] was also used in this work.

ν	q
0	10^4
1	10^4
2	10^4
3	-1.91
4	-2.72
5	-2.72
6	-2.62
7	-3.71
8-17	-9.3

5.4 Gaussian Convolution

In order to further improve the line shape from the simulation, and to correctly fit the experimental lines to get an estimate for the q parameter, the introduction of the experimental resolution was also needed. The implemented algorithm consists in convolving the simulated signal with a Gaussian, which standard deviation corresponds to the expected from the experimental resolution.

In order to account for the experimental resolution, the experimental data is fitted to a Fano-line shape, as given in equation (39), convolved with a Gaussian function. This fit was necessary to obtain the correct values of the q parameters used in the previous section. In the fig.25, a fit of one of the experimental lines is shown. Two values for the q value are given: one was calculated letting the experimental resolution σ fixed in the expected range of the experimental resolution, and the other one let σ also be a free-fit parameter. The two results are very similar. Each of the lines is fitted in order to get their individual q parameters in the case of no NIR light. For the σ-parameter estimate, a fit of the $D_{\nu=3}$ line was chosen, since is the most visible line in the experimental data, obtaining a value of $\sigma = 0.0036$ eV. The expected range for σ from the experimental side was 1-5 meV, being the fitted value in the accepted range. Therefore, all further analysis is performed with the convolution of the simulated signal as estimated to be of value $\sigma = 0.0036$ eV.

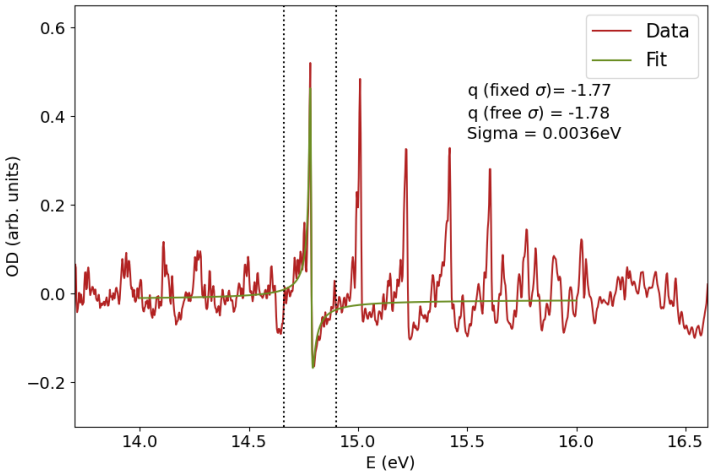

Figure 25: Example of fitting of the experimental data for the $D_{\nu=3}$ line. For the Fano-parameter, two methods were used. The first q value presented corresponds to a fit with fixed $\sigma = 1$ meV. The second q value is obtained by letting σ be also a free fit parameter. The two results are almost identical. The fitted value of $\sigma = 3.6$ meV will be used in this section to convolve the data with a Gaussian function.

Note, however, that the convolution could not be applied directly to the calculated optical density. The correct procedure is to apply the convolution to the simulated signal, S, as explained in more detail in [28]. The steps for this procedure are:

1. Calculate the non-convoluted optical density as usual from the simulation.
2. Following equation (1), calculate the signal as $I(\omega) = I_0(\omega)10^{-\mathrm{OD}(\omega)}$. For the reference $I_0(\omega)$, the spectrum of the XUV pulse is taken.
3. Get the convolved signal as $I_{\mathrm{conv}}(\omega) = (I * \mathcal{N}(\mu, \sigma^2))(\omega)$. Note that for the convolution, the central value of the Gaussian μ is not relevant.
4. Calculate the new optical density as $\mathrm{OD}_{\mathrm{conv}} = -log_{10}\left(\frac{I_{\mathrm{conv}}(\omega)}{I_0(\omega)}\right)$.

In fig.26, the results for the convoluted lines are presented. For low intensities of the NIR light, the convolution shows the desired effect. It broadens the lines and reduces the intensity of the first three lines, which line shape, recall, was not adapted with the Fano phase because they are below the dissociation energy of the B states. For higher intensities of the NIR light, the lines which had a Fano phase (with $\nu > 2$) still look very much like in the experiment. However, the simulated lower lines accumulate large populations and start emitting, which is not corresponding to the experimental results. This effect indicates that, most likely, the lifetime of those lines is too long for the correct functioning of the simulation. When trying to increment their lifetime by broadening the lines, however, the time-dependent dipole moment

did not decay until really long times. The decay of the dipole moment is necessary in order to calculate the optical density as its Fourier transform. Tapering the dipole moment to perform the Fourier transform is not providing satisfying results, as shown in fig.27 for a lifetime of 2418 fs, 10 times bigger than before (corresponding to $\Gamma = 1e^{-5}$ a.u.), and with the tapering function being a flat function with squared cosine functions on the sides. For this reason, it was decided to leave the simulated lines like that, since the first lines are also not that visible in the experiment for lower NIR light, but it is important to keep in mind this consideration when interpreting figure 26. Due to the too long lifetime included in the simulation, population accumulates in those states and emission is to be seen in the simulated results, which does not correspond to the experimental observations.

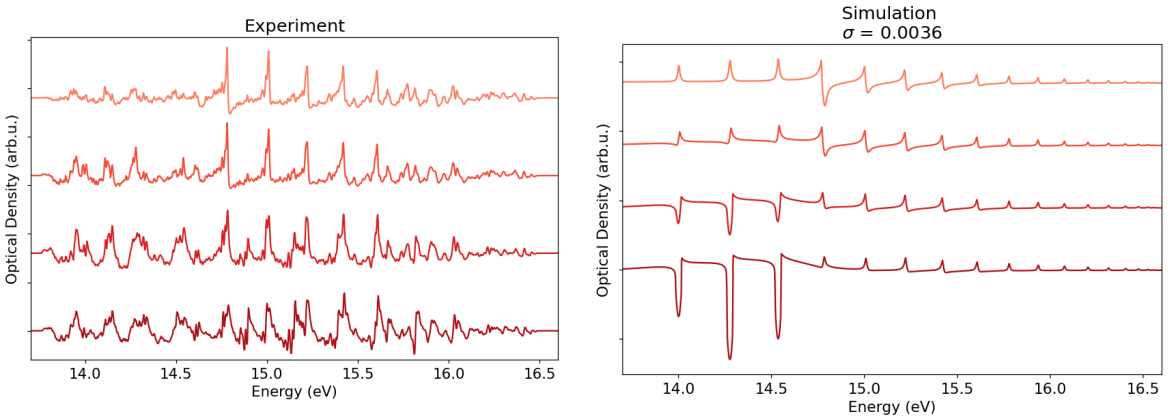

Figure 26: Optical Density from experiment and simulation for increasing (lighter to darker red) NIR Intensity and including both the Fano phases and the Gaussian convolution. The lines which included the Fano Phases ($\nu > 2$) correspond now in position and also in line width to the experimental results. For the lines in which no Fano Phase was included in the simulation, emission is produced, which is a hint of a too long simulated lifetime.

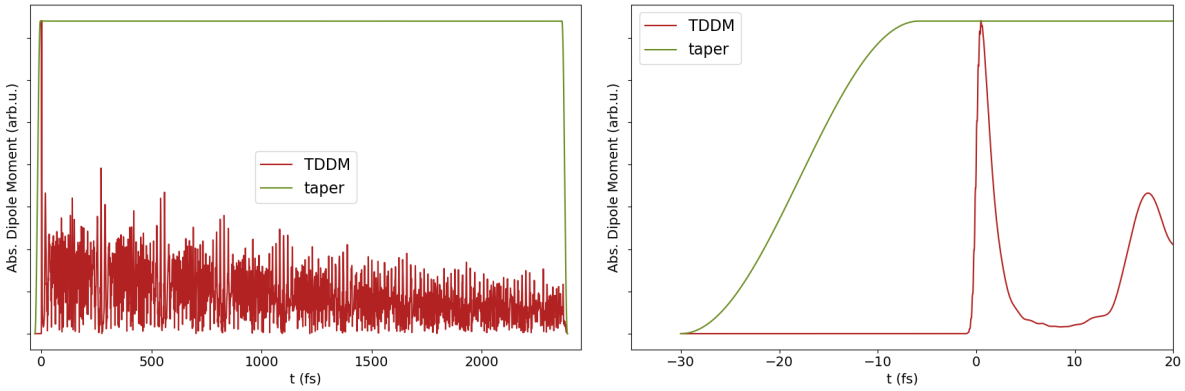

Figure 27: Time-dependent dipole moment when giving the first states a longer lifetime ($\Gamma = 1e^{-5}$ a.u.). The taper, which in this case is a flat function with squared cosine rising and falling sides, is also shown. The taper ensures that the dipole goes to zero on the sides in order to correctly perform a Fourier transform. However, the transformation is no longer smooth. On the right, a zoomed version for the earlier times is shown, in order to clearly show the squared cosine rising side. The falling side would be completely simetrical.

5.5 Time-Delay study

The time at which the NIR light interacts with the hydrogen molecule, the so-called time delay, has an influence on the system evolution and on the revival quality. In the following section, the results for a study with varying time delay, τ, and constant NIR intensity are presented.

In fig.28, the time-dependent dipole moment is plot with respect to the real time in the x-axis and the time delay at which the NIR light arrives to the H_2 molecule in the y-axis. In this case, the mid-strong value of $3.5\dot{1}0^{12}\,\mathrm{W/cm^2}$ was chosen for the NIR intensity. As expected, no big changes are produced when the Time Delay (TD) is negative. This is due to the fact, that the XUV light has not yet excited any population when the NIR light arrives, and therefore, no interaction between levels is caused by the NIR light. This case is equivalent to no NIR light. However, for positive time delays, a line of slope unity can be observed, as a result of the system perturbation caused by the NIR light. This perturbation is more visible in the zoomed picture on the right.

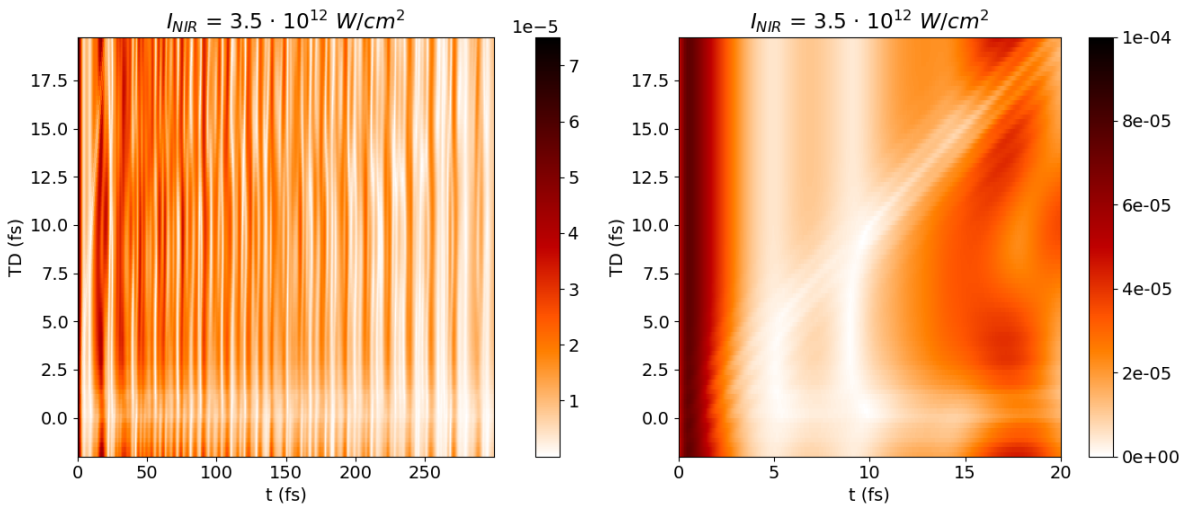

Figure 28: Time-dependent dipole moment with respect to the real time (x-axis) and the TD (y-axis). For negative time delays, the system does not suffer a perturbation caused by NIR light. For positive time delays, the perturbation is to be seen as a line of slope one. The picture on the right is a zoomed version, where this line can better be observed.

In fig.29, the zoomed picture focuses on the revival time. Here, a very interesting effect occurs. For negative TD, again, the NIR has no influence on the system. However, for positive TD, clear changes in the revival are observed. For small (but positive) τ, the revival has a defined position. For later time delays, around 9 fs, the revival loses definition, and splits in two bumps. This effect could already be seen in the previous section studying the effect of the NIR light, since the time delay used there was $\tau = 7$ fs. Moreover, for even longer time delays ($\tau \sim 18$ fs), the definition of the revival is recovered.

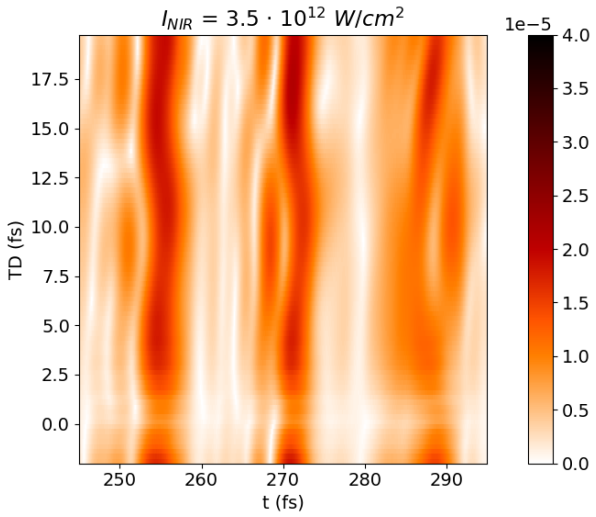

Figure 29: Zoomed version of the time-dependent dipole moment around the expected revival time, with respect to the real time (x-axis) and the TD (y-axis). The revival, seen as the recovery of regularity of the TDDM is to be observed, but its definition is different for different TD. For small (but positive) TD, the revival has a defined position. For later time delays, around 9fs, the revival loses definition, and splits in two bumps. And for even longer time delays ($t \sim 18$ fs), the definition of the revival is recovered.

In order to investigate these phenomena further, results from section 5.1 are recalled here. By looking at fig.14, one can see how the wavepacket, after its creation, starts oscillating in space. It is created exactly centred in the Franck-Condon region, but it travels until the two nuclei are separated a distance of around $2\mathring{A}$, to then go back to the original position, followed by further oscillations. One full oscillation back and forth in space takes the wavepacket around 18 fs. As it can be seen in the fig.13, which shows the potential curves and the wavepacket at $t = 0$ (when it is first created), the potential curve for the EF states, which are the ones receiving population via the NIR coupling, has two wells. Therefore, it looks very different in the Frack-Condon region, where it could be approximated by a simple well potential, than at bigger nuclear separation coordinates, where the potential curve presents a bump and the second well.

There is one remarkable feature about the wavefunctions of the EF energy levels. As it is shown in fig.30, the lowest energy levels present wave functions that resemble very much the ones that would be expected for a harmonic oscillator, and each of the levels has an increased probability of belonging to either the first or the second well. So for example, the levels with $\nu = 0$ and 3 have a high probability density in the first well, whereas the levels $\nu = 1$, 2, 4 and 5 could be said to belong to the second potential well. Since the first well is narrower, its energy levels are further spaced in energy. For higher energy levels, like $\nu = 7$, the wave function has maxima in both wells. This is the case for all levels with $\nu > 7$. Notice that

some levels present a probability maxima on top of the bump of the potential curve, which is specially relevant for levels ν =6 and 9. For higher $\nu > 10$, a regular maxima and minima structure is observed.

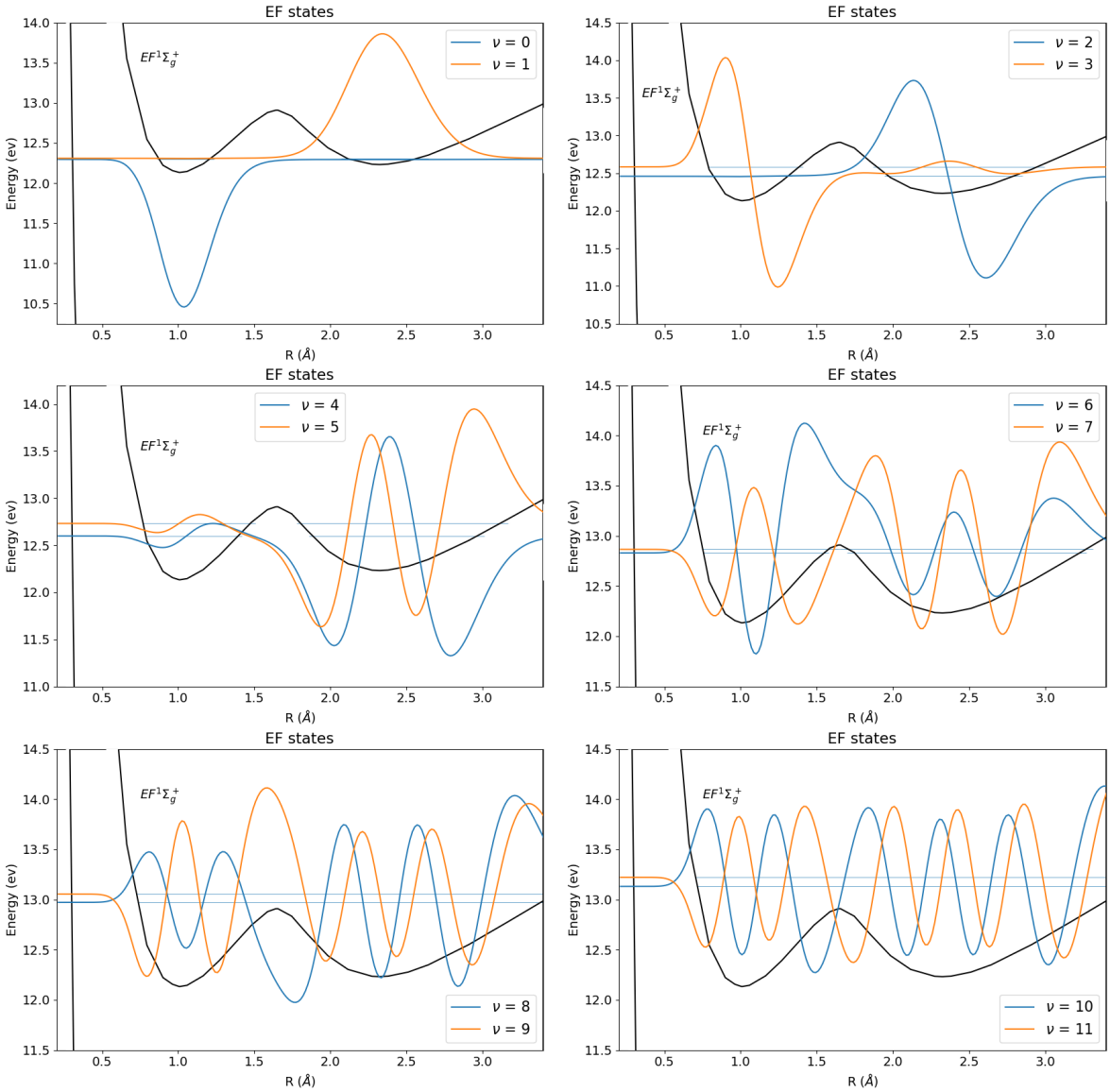

Figure 30: Wavefunctions of the lower energy levels of the EF-potential curve. The lowest ones clearly belong to either the first or the second well of the potential, and resemble the ones expected for a harmonic oscillator. For levels with $\nu = 7$ or above, this separation in one of the potential wells is no longer possible. Note, levels $\nu = 6$ and 9 present a maxima in the bump of the potential curve.

With this structure of the wavefunctions in mind, fig.31 presents the wavepacket of the EF energy states created for each time delay at $t = \tau$, meaning, at the time when the EF wavepacket is created, since the population can only access those levels when the NIR pulse arrives. This wavepacket is equivalent to the one shown in previous sections, but refers to the EF states and not to the D states. In the picture, the Frank-Condon region *of the D states* is also shown, in order to situate where the initial wavepacket, which for the EF states is the D wavepacket, is created around $t = 0$.

As it can be seen in this picture, for small time delays, $0 < \tau < 3$ fs, the EF-wavepacket is created very close to the first potential-well minimum, around $R = 1\mathring{A}$. For later time delays, around $\tau \sim 17$fs, it can again be observed that the wavepacket has a Gaussian structure around $R = 1\mathring{A}$. However, for intermediate values of the time delay, a high population density is observed around $R = 1.5\mathring{A}$, closer to the EF-potential bump. The maximum displacement takes place at $\tau = 9$fs. Note as well that for $\tau \sim 9$fs and $\tau \sim 17$fs, the EF wavepacket is specially populated. In a classical picture, this is due to the deceleration of the D wavepacket at those specific times, which are the turning points on the wave-packet oscillation. The D wavepacket has then no kinetic energy and the coupling to the EF states is very efficient.

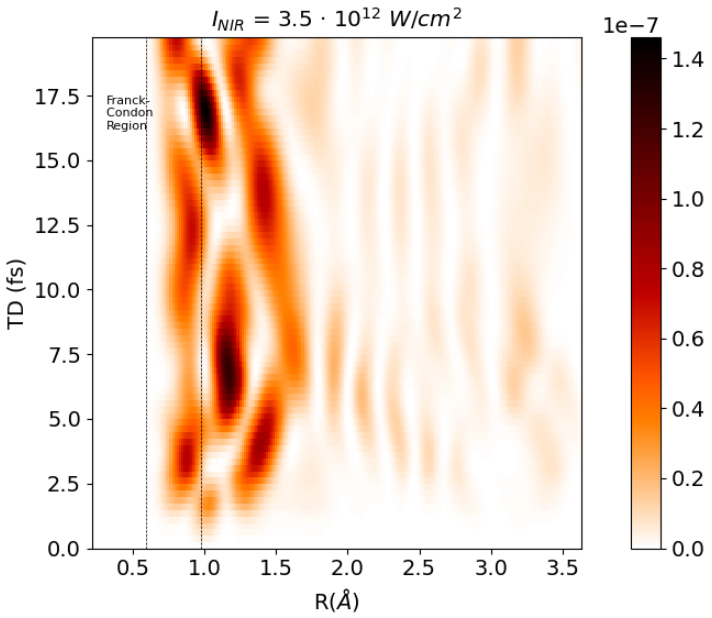

Figure 31: Spatial representation of the EF wavepacket at its creation time, i.e., at $t = \tau$ for different time delays. Note, that the time at which the wavepacket is plot varies then of course with the TD. For small time delays ($0 < \tau < 3$ fs) as well as for larger time delays (around $\tau \sim 17$fs), the EF wavepacket is a defined Gaussian around the potential minimum $R = 1\mathring{A}$. For these time-delays, the revival of the wavepacket was well-defined. However, in-between time delays, some population density appears nearer to the EF-potential maximum, at around $1.5\mathring{A}$. The major revival distortion is given for time delay $\tau = 9$fs, for which most of the population is created away from the $R = 1\mathring{A}$ position. Notice also how the population transfer is specially more efficient at $\tau = 9$ and 17fs. These are the turning points of the D wavepacket. The D wavepacket stays longer in the same position, which makes the coupling to the EF states more efficient.

This effect can also be analysed by looking at the EF states which couple the most to the D wavepacket, or in other words, which receive the most population. This is presented in fig.32. It represents the square of the population coefficients for the EF states, meaning, the probability that a particular state is populated. The coefficients are defined in equation (55). In this plot, one can observe how the states with $\nu = 0$ and 3 are the most populated for all time delays. This makes sense, since the D wavepacket travels most of the time above the first well, which favours the interaction with the levels that belong to the first well. The levels that belong exclusively to the second well, like $\nu = 1$, 2, 4 and 5 are barely populated. No overlap of the nuclear wavefunctions of D and these levels takes place. Notice that the population transfer is not instantaneous at $t = \tau$, but that the NIR pulse has a time duration of around 5fs.

Furthermore, two levels are of relevance in the central region of our time delays, the levels

$\nu = 6$ and 9. These two levels have a high population density on top of the EF-potential bump, and the D-wavepacket is travelling around that position at those times. The fact that these two levels get involved distorts the wavepacket of the EF states. Notice that these two levels also have population probability densities in the second well. This causes, as observed in figure 31, a spreading of the EF wavepacket. The D and EF interaction loses regularity. And of course, this affects the phases of the D states, causing the observed revival distortion.

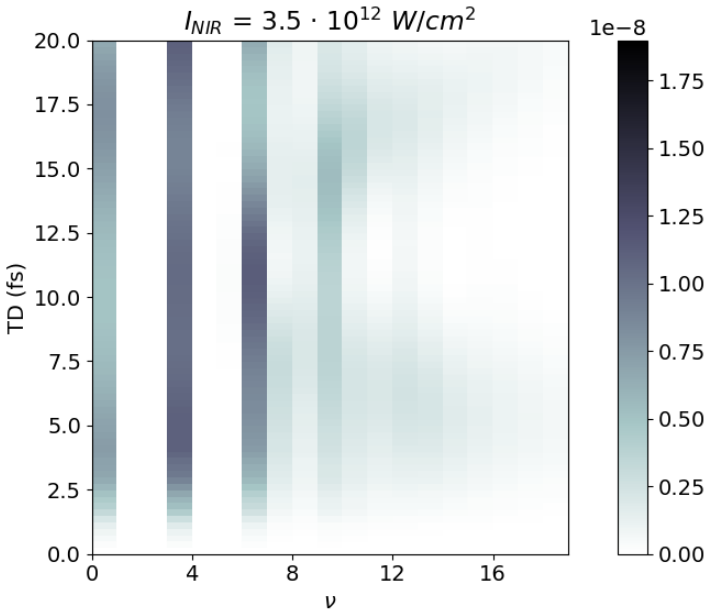

Figure 32: Square of the population coefficient (i.e. population probability) for the different EF states at $t = \tau$ for different time delays. The states of the first well ($\nu = 0$, and 3) are always populated by the NIR light, while the ones belonging almost exclusively to the second well ($\nu = 1$, 2, 4, and 5) are barely populated. Of particular interest are the states causing the revival distortion for central time delays. One can observe that the states $\nu = 6$ and 9 are then more populated than when the D-wavepacket is in its Franck-Condon region. The fact these EF states are populated causes the spreading of the EF packet and the distortion of the D-wavepacket revival.

To conclude the time-delay study, some results about the added phase to the D-wavepacket caused by the NIR light are presented. In fig.33, the accumulated phases for the bound levels of the D potential curve are shown for NIR intensity of $3.5 \times 10^{16}\,\mathrm{W/cm^2}$. This phase accumulation is caused by the NIR pulse. In the picture, the accumulated phase of the natural time evolution of the states is removed by subtracting the reference with no NIR light. For a small time delay, when the two pulses come very close to each other, the less energetic a level is, the more accumulated phase it becomes. The phase-addition induced by the NIR light is

what causes the revival time to be shifted to earlier times.

The regularity observed in the extra phase for lower time delays is lost for later time delays. For time delays $\tau = 6$ and 9 fs, one starts seeing how the $\nu = 1$ level gets a greater added phase than the $\nu = 0$ level. Moreover, with increasing time delay, some of the levels start getting positive added phase, which does not follow the previous trend any more. This shows again the new interactions that start happening with other EF-levels when the D-wavepacket is travelling outside its Franck-Condon region as the NIR pulse arrives, increasing the complexity of the system. The loss in regularity on the accumulated phase distorts the revival time, and as it was shown previously, the revival looses on definition for time delays around $\tau = 9$ fs.

At $\tau = 18$ fs, the regularity is recovered for the lower levels, but some levels still have inverted phase signs. However, since the lower levels are the ones contributing the most in the creation of the wavepacket, the revival is again very well-defined.

Part of the intention when showing this picture is also to show the complexity of the phase study. Many aspects of these plots raise questions that could be used to continue this research in different directions. Some ideas for it will be presented in the following summarizing section.

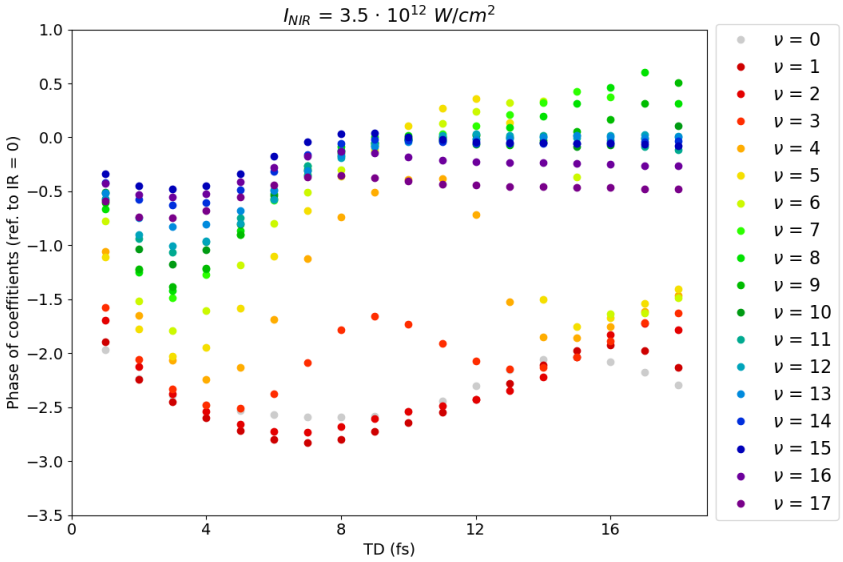

Figure 33: Accumulated phases of the first bound levels of the D wavepacket for different time delays. The regularity of the earlier time delays, where the less energetic levels get respectively a bigger (in absolute value) accumulated phase, is distorted when the NIR comes at a later time. From $\tau = 12$fs, some of the levels get a positive added phase, opposite to the general tendency. For $\tau = 18$fs, the regularity is not completely recovered. However, attending to the previous results, it seems that the added phases still allow for a defined revival to take place.

6 Conclusions

The aim of this project was to perform multi-level simulations based on the quantum theory for light-matter interaction in order to study an absorption experiment with two laser pulses, one XUV and one NIR pulse, and molecular hydrogen as target. The simulations were used to recreate experimental results, as well as to study further effects that could not be directly measured.

The first steps consisted in gathering the required information on the energy levels and the nuclear wavefunctions of the hydrogen molecule. For this, two external codes, *nucfix* and *rovib_trans*, were used. Using the potential curves obtained from literature, the codes solved the time-independent Schrödinger Equation and delivered the desired information. Moreover, the overlap between wavefunctions, taking into account the $R-$dependent couplings, was also calculated, obtaining then the transition probabilities between the different levels.

After gathering these values, the simulations of the time evolution could be performed. The wavepacket of the D-levels was calculated using the transition probabilities, and with the time-dependent Schrödinger equation, also its time evolution could be computed. The revival of the wavepacket at $t \sim 272$fs was observed, very well-defined for the case when no NIR light was acting on the system, and perturbed when some NIR light interacted with the hydrogen target.

Two experimental variables were calculated in the simulation and compared with the ones obtained from measured data: the time-dependent dipole moment and the optical density. In both experimental and simulated results for the dipole moment, the very interesting phenomenon of the revival time shift was observed. With increasing NIR intensity, the revival was shifted to earlier time, due to the accumulated phase in the time evolution brought by the NIR field. This feature could be a hint for revival time control, and it is one of the most exciting results of the project.

For the optical density, experimental and simulated data were in good agreement for the line position. However, the line shape of the experiment was not reproduced. The Fano theory for bound states embedded in a continuum was introduced, in the equivalent form of the theory which makes use of the so-called Fano phases. By fitting only the case with no NIR light to the experimental results to get the appropriate values for the q-parameters, the experimental line shape was recovered in the simulation also for higher NIR intensity values. The simulated line shape was also corrected by convolving a Gaussian function, which represented the limited experimental resolution.

Finally, a time-delay study with constant NIR intensity was also performed. One could observe how the revival definition depended on the position of the D-wavepacket at the mo-

ment of the NIR-pulse arrival. If the D-wavepacket was in the Franck-Condon region (meaning also that it was far away from the second well of the EF potential), the revival is very well-defined. However, when the wavepacket travels outside its Franck-Condon region, for example at the turning point at $t = 9$ fs, the revival gets a splitting and loses resolution. By studying the nuclear wavefunctions of the EF energy levels, it could be seen that several levels that were present in both wells of the EF potential curve were more populated when the D-wavepacket's nuclear coordinate had a higher value at the interaction time, τ. On the contrary, when the D-wavepacket was in the Franck-Condon region, the EF-levels that interacted the most were the ones which had the highest probability in the first potential well. To show the difficulties of the problem, the NIR-added phase to the D levels for different time delays was also plot. In this part of the study, one could see how the added phase lost regularity, or even changed sign for increasing time delays. This aspect shows the complexity of the problem. Further analysis on the topic could investigate more the effects of the NIR-added phase.

Summarizing, the project explored many aspects of the strong-field effects on singly excited vibronic resonances in the hydrogen molecule. The experimental results could then be compared with the theory, finding general agreement, and aspects that could not be recovered from the measured data could also be studied.

Many experimental results could be recovered by using only the minimum number of levels in the simulation, being this the goal of the project. Of course, there are still many other aspects of the system that could further be studied. Significantly longer simulations could be performed in order to be able to implement the longer lifetime needed to avoid emission from the lowest levels, a problem that was left opened in section 5.3.3. In this regard, other possible implementations of the taper could also be considered. The study of the phases and its change due to the NIR interaction could further be analysed, for example, looking at the extreme case of delta shaped pulses. Moreover, other potential curves and their levels could be included in the simulation. Some absorption lines corresponding to C levels are to see in the experimental results, so their inclusion would improve the simulation. In conclusion, the field still offers many interesting research directions that could further be explored.

References

1. Maiman, T. H. “Stimulated optical radiation in ruby”. *Nature* **187,** 493–494 (1960).
2. Clauser, J. F., Horne, M. A., Shimony, A. & Holt, R. A. “Proposed Experiment to Test Local Hidden-Variable Theories”. *Physical Review Letter* **23,** 880–884 (1969).
3. Aspect, A., Grangier, P. & Roger, G. “Experimental Realization of Einstein-Podolsky-Rosen-Bohm Gedankenexperiment: A New Violation of Bell’s Inequalities”. *Physical Review Letter* **49,** 91–94 (1982).
4. Aspect, A., Dalibard, J. & Roger, G. “Experimental Test of Bell’s Inequalities Using Time-Varying Analyzers”. *Physical Review Letter* **49,** 1804–1807 (1982).
5. Giustina, M. *et al.* “Significant-Loophole-Free Test of Bell’s Theorem with Entangled Photons”. *Physical Review Letter* **115,** 250401 (2015).
6. Stooß, V., Hartmann, M., Birk, P., Borisova, G. D., Ding, T., Blättermann, A., Ott, C. & Pfeifer, T. “XUV-beamline for attosecond transient absorption measurements featuring a broadband common beam-path time-delay unit and in situ reference spectrometer for high stability and sensitivity”. *Review of Scientific Instruments* **90,** 053108 (2019).
7. Goulielmakis, E., Loh, Z.-H., Wirth, A., Santra, R., Rohringer, N., Yakovlev, V. S., Zherebtsov, S., Pfeifer, T., Azzeer, A. M., Kling, M. F. & et al. “Real-time observation of Valence Electron Motion”. *Nature* **466,** 739 (2010).
8. Mauritsson, J. *et al.* “Attosecond Electron Spectroscopy Using a Novel Interferometric Pump-Probe Technique”. *Physical Review Letter* **105,** 053001 (2010).
9. Holler, M., Schapper, F., Gallmann, L. & Keller, U. “Attosecond Electron Wave-Packet Interference Observed by Transient Absorption”. *Physical Review Letter* **106,** 123601 (2011).
10. Ott, C., Kaldun, A., Argenti, L., Raith, P., Meyer, K., Laux, M., Zhang, Y., Blättermann, A., Hagstotz, S., Ding, T. & et al. “Reconstruction and control of a time-dependent two-electron wave packet”. *Nature* **516,** 374 (2014).
11. Sansone, G., Kelkensberg, F., Pérez-Torres, J. F., Morales, F., Kling, M. F., Siu, W., Ghafur, O., Johnsson, P., Swoboda, M., Benedetti, E. & et al. “Electron localization following attosecond molecular photoionization”. *Nature* **465,** 763 (2010).
12. Calegari, F., Ayuso, D., Trabattoni, A., Belshaw, L., De Camillis, S., Anumula, S., Frassetto, F., Poletto, L., Palacios, A., Decleva, P., Greenwood, J., Martín, F. & Nisoli, M. “Ultrafast Electron Dynamics in phenylalanine initiated by attosecond pulses”. *Science (New York, N.Y.)* **346,** 336 (2014).

13. Cao, W., Warrick, E. R., Fidler, A., Leone, S. R. & Neumark, D. M. “Excited-state vibronic wave-packet dynamics in H_2 probed by XUV transient four-wave mixing”. *Physical Review A* **97,** 023401 (2018).

14. Schmidt, P., Knie, A., Hans, A., Hosaka, K., Ukai, M., Glass-Maujean, M. & Ehresmann, A. “Photon-excitation photon-emission maps (PhexPhem maps) with rovibronic resolution as a data base for theory and astrophysics part I: method and first results for H_2”. *Journal of Physics B: Atomic, Molecular and Optical Physics* **54,** 034001 (2021).

15. Chan, W., Cooper, G. & Brion, C. “Absolute optical oscillator strengths (11–20 eV) and transition moments for the photoabsorption of molecular hydrogen in the Lyman and Werner bands”. *Chemical Physics* **168,** 375–388 (1992).

16. Cheng, Y., Chini, M., Wang, X., González-Castrillo, A., Palacios, A., Argenti, L., Martın, F. & Chang, Z. “Reconstruction of an excited-state molecular wave packet with attosecond transient absorption spectroscopy”. *Physical Review A* **94,** 023403 (2016).

17. Bandrauk, A. D. & Shen, H. “Improved exponential split operator method for solving the time-dependent Schrödinger equation”. *Chemical Physics Letters* **176,** 428–432 (1991).

18. Feuerstein, B., Ergler, T., Rudenko, A., Zrost, K., Schröter, C., Moshammer, R., Ullrich, J., Niederhausen, T. & Thumm, U. “Complete characterization of molecular dynamics in Ultrashort Laser Fields”. *Physical Review Letter* **99,** 153002 (2007).

19. Brinks, D., Stefani, F. D., Kulzer, F., Hildner, R., Taminiau, T. H., Avlasevich, Y., Müllen, K. & van Hulst, N. F. “Visualizing and controlling vibrational wave packets of single molecules”. *Nature* **465,** 905 (2010).

20. Okino, T., Furukawa, Y., Nabekawa, Y., Miyabe, S., A., A., Amani Eilanlou, A., E.J., T., Yamanouchi, K. & Midorikawa, K. “Direct Observation of an Attosecond Electron Wave Packet in a Nitrogen Molecule”. *Science Advances* **1** (2015).

21. Timmers, H., Zhu, X., Li, Z., Kobayashi, Y., Sabbar, M., Hollstein, M., Reduzzi, M., Martínez, T., Neumark, D. & Leone, S. “Disentangling conical intersection and coherent molecular dynamics in methyl bromide with attosecond transient absorption spectroscopy.” *Nature Communications* **10,** 3133 (2019).

22. Karamatskos, E. T., Raabe, S., Mullins, T., Trabattoni, A., Stammer, P., Goldsztejn, G., Johansen, R. R., Długołecki, K., Stapelfeldt, H., Vrakking, M. J. J., Trippel, S., Rouzée, A. & Küpper, J. “Molecular movie of ultrafast coherent rotational dynamics of OCS”. *Nature Communications* **10,** 3364 (2019).

23. Sussman, B. J., Townsend, D., Ivanov, M. Y. & Stolow, A. “Dynamic stark control of photochemical processes”. *Science* **314,** 278–281 (2006).

24. Peng, P., Mi, Y., Lytova, M., Britton, M., Ding, X., Naumov, A. Y., Corkum, P. B. & Villeneuve, D. M. “Coherent Control of Ultrafast Extreme Ultraviolet Transient Absorption”. *Nature Photonics* **16,** 45 (2022).

25. Vrakking, M. J. J., Villeneuve, D. M. & Stolow, A. “Observation of fractional revivals of a molecular wave packet”. *Physical Review A* **54,** R37–R40 (1996).

26. Ergler, T., Rudenko, A., Feuerstein, B., Zrost, K., Schröter, C. D., Moshammer, R. & Ullrich, J. “Spatiotemporal Imaging of Ultrafast Molecular Motion: Collapse and Revival of the $D_2{}^+$ Nuclear Wave Packet”. *Physical Review Letter* **97,** 193001 (2006).

27. Borisova, G. D., Barber Belda, P., Hu, S., Birk, P., Stooß, V., Hartmann, M., Fan, D., Saenz Alejandro Ott, C. & Pfeifer, T. “Strong-field control of a vibrational wavepacket”. In preparation.

28. Birk, P. “The Dipole Response of an Ionization Threshold within Ultrashort and Strong Fields”. PhD thesis (Heidelberg University, 2020).

29. Hertel, I. V. & Schulz, C. “Atoms, Molecules and Optical Physics 2” (Springer, 2015).

30. Fano, U. “Effects of Configuration Interaction on Intensities and Phase Shifts”. *Physics Review* **124,** 1866–1878 (1961).

31. Saenz, A. “nufix.f90”. Institut für Physik, Humboldt-Universität zu Berlin. Last modified: 11.03.2004.

32. Saenz, A. “rovib_trans.f90”. Institut für Physik, Humboldt-Universität zu Berlin. Last modified: 19.03.2004.

33. Sharp, T. E. “Potential-Energy Curves for Molecular Hydrogen and Its Ions”. *Atomic Data and Nuclear Data Tables* **2,** 119–169 (1970).

34. Wolniewicz, L. & Staszewska, G. “$^1\Sigma_u \rightarrow \mathrm{X}\ ^1\Sigma_g^+$ transition moments for the hydrogen molecule”. *Journal of Molecular Spectroscopy* **217,** 181–185 (2003).

35. Wolniewicz, L. & Staszewska, G. “Excited $^1\Pi_u$ states and the $^1\Pi_u \rightarrow \mathrm{X}\ ^1\Sigma_g^+$ transition moments of the hydrogen molecule”. *Journal of Molecular Spectroscopy* **220,** 45–51 (2003).

36. Fan, D. “A few-level simulation of the time-dependent dynamics of singly excited resonances of molecular hydrogen under the influence of moderately strong, ultrashort laser pulses”. BSc Thesis (Heidelberg University, 2020).

37. Stooß, V., Cavaletto, S. M., Donsa, S., Blättermann, A., Birk, P., Keitel, C. H., B řezinová, I., Burgdörfer, J., Ott, C. & Pfeifer, T. “Real-Time Reconstruction of the Strong-Field-Driven Dipole Response”. *Physical Review Letter* **121,** 173005 (17 2018).

38. Kaldun, A., Ott, C., Stooß, V., Fischer, A., Blättermann, A., Ding, T., Raith, P., Meyer, K., Laux, M., Evers, J., Keitel, C., Greene, C. & Pfeifer, T. “Fano Resonances in the Time Domain”. *Journal of Physics: Conference Series* **635,** 092079 (2015).

39. Kaldun, A., Ott, C., Blättermann, A., Laux, M., Meyer, K., Ding, T., Fischer, A. & Pfeifer, T. “Extracting Phase and Amplitude Modifications of Laser-Coupled Fano Resonances”. *Physical Review Letter* **112,** 103001 (2014).

40. Dickenson, G. D., Ivanov, T. I., Roudjane, M., de Oliveira, N., Joyeux, D., Nahon, L., Tchang-Brillet, W.-Ü. L., Glass-Maujean, M., Haar, I., Ehresmann, A. & Ubachs, W. “Synchrotron vacuum ultraviolet radiation studies of the $D^1\Pi_u$ state of H_2”. *The Journal of Chemical Physics* **133,** 144317 (2010).

41. Borisova, G. D. “Theoretical and Experimental Studies of XUV Multielectron (Auto-) Ionization Dynamics in Helium and Molecular Hydrogen”. MSc Thesis (Heidelberg University, 2017).

42. Glass-Maujean, M., Breton, J. & Guyon, P. “A fano-profile study of the predissociation of the 3p $D^1\Pi_u^+$ state of H_2”. *Chemical Physics Letters* **63,** 591–595 (1979).

Acknowledgments

This thesis would not have been possible without the help of many people that supported me in various (and all indispensable) ways in the process.

First, to the person that worked with me day to day, **Gergana D. Borisova**. Thanks for your ideas, your encouragement and your patience.

To my supervisors, **Pr. Dr. Thomas Pfeifer** and **Dr. Christian Ott**. You taught me a lot during this year. Thanks for your help. Also, to **Pr. Dr. Alejandro Saenz**, for providing the essential theoretical insights.

To the people in the group, **Marc Rebholz, Lennart Aufleger, Patrick Rupprecht, Shuyuan Hu, Carina da Costa Castanheira, Alexander Magunia, Yu He, Finn Lubenau, Daniel Richter, Felix Klein, Maximilian Richter**. Although the pandemic made personal contact difficult during the year, thanks for your help and for the nice lunch breaks.

To everyone that helped me somehow during the year.

To my father **Xavi**, to my mother, **Amparo**, to **Sonia** and to **Nuria**. Thank you for always being there for me.

To **Etienne**. Thank you for being always (literally) there. Thanks for showing up in the right moment. And, of course, for staying.

And always, to **Sasha**.

Erklärung:

Ich versichere, dass ich diese Arbeit selbstständig verfasst habe und keine anderen als die angegebenen Quellen und Hilfsmittel benutzt habe.

Heidelberg, den 17.10.2022 . . . . . .